Remote Sensing of Environment 204 (2018) 534–552

Contents lists available at ScienceDirect

Remote Sensing of Environment

journal homepage: www.elsevier.com/locate/rse

Detecting geothermal anomalies and evaluating LST geothermal component by combining thermal remote sensing time series and land surface model data

Romaguera M.[a,*], Vaughan R.G.[b], Ettema J.[a], Izquierdo-Verdiguier E.[a], Hecker C.A.[a], van der Meer F.D.[a]

[a] Faculty of Geo-Information Science and Earth Observation (ITC), University of Twente, Hengelosestraat 99, P.O. Box 217, Enschede 7500AE, The Netherlands
[b] US Geological Survey, Astrogeology Science Center, Flagstaff, AZ, USA

ARTICLE INFO

Keywords:
Geothermal
Land surface temperature
Remote sensing
Land surface model
Kenyan Rift

ABSTRACT

This paper explores for the first time the possibilities to use two land surface temperature (LST) time series of different origins (geostationary Meteosat Second Generation satellite data and Noah land surface modelling, LSM), to detect geothermal anomalies and extract the geothermal component of LST, the LST_{gt}. We hypothesize that in geothermal areas the LSM time series will underestimate the LST as compared to the remote sensing data, since the former does not account for the geothermal component in its model.

In order to extract LST_{gt}, two approaches of different nature (physical based and data mining) were developed and tested in an area of about 560 × 560 km^2 centered at the Kenyan Rift. Pre-dawn data in the study area during the first 45 days of 2012 were analyzed.

The results show consistent spatial and temporal LST_{gt} patterns between the two approaches, and systematic differences of about 2 K. A geothermal area map from surface studies was used to assess LST_{gt} inside and outside the geothermal boundaries. Spatial means were found to be higher inside the geothermal limits, as well as the relative frequency of occurrence of high LST_{gt}. Results further show that areas with strong topography can result in anomalously high LST_{gt} values (false positives), which suggests the need for a slope and aspect correction in the inputs to achieve realistic results in those areas. The uncertainty analysis indicates that large uncertainties of the input parameters may limit detection of LST_{gt} anomalies. To validate the approaches, higher spatial resolution images from the Advanced Spaceborne Thermal Emission and Reflection Radiometer (ASTER) data over the Olkaria geothermal field were used. An established method to estimate radiant geothermal flux was applied providing values between 9 and 24 W/m^2 in the geothermal area, which coincides with the LST_{gt} flux rates obtained with the proposed approaches.

The proposed approaches are a first step in estimating LST_{gt} at large spatial coverage from remote sensing and LSM data series, and provide an innovative framework for future improvements.

1. Introduction

Thermal infrared remote sensing (RS) and the derived land surface temperature (LST) can be used for geothermal applications to map thermal anomalies and calculate the geothermal heat flux (Haselwimmer and Prakash, 2013; Ramsey and Harris, 2013; van der Meer et al., 2014). Although most of the published literature has focused on the use of airborne thermal imagery with high spatial resolution (i.e. < 5 m) during the last decade several authors have worked on the use of medium resolution thermal imagery from Advanced Spaceborne Thermal Emission and Reflection Radiometer (ASTER), Landsat and Moderate Resolution Imaging Spectroradiometer (MODIS) (90 m, 120 m, and 1 km spatial resolution respectively).

Coolbaugh et al. (2007) used ASTER thermal imagery to map geothermal anomalies at Bradys Hot Springs (US). The method aimed to minimize temperature variations caused by the diurnal heating effects of the sun in order to highlight subsurface contributions of geothermal heat. A pseudo-temperature image was created after the correction of albedo, terrain slope, and thermal inertia effects.

Eneva and Coolbaugh (2009) used ASTER imagery and elaborated on the importance of incorporating nighttime temperature inversions, along with the effects of elevation when using thermal remote sensing

* Corresponding author.
E-mail address: mireia.romaguera@uv.es (M. Romaguera).

https://doi.org/10.1016/j.rse.2017.10.003
Received 27 November 2016; Received in revised form 19 September 2017; Accepted 5 October 2017
Available online 11 November 2017
0034-4257/

for geothermal activity detection. Gutierrez et al. (2012) implemented this improvement by including altitude in thermal anomaly detection in the geothermal complexes of the Andes (Central Chile).

Watson et al. (2008) used a simplified surface energy balance equation and Landsat data to calculate a 'residual terrestrial emittance anomaly' throughout Yellowstone National Park that clearly discriminated geothermal from non-geothermal areas. The resulting values provided a lower bound on geothermal heat flux for that system, with values between 0 and 94 W/m^2.

Vaughan et al. (2012) analyzed ASTER and MODIS thermal data at the Yellowstone National Park acquired in the 2000–2010 period. The method identified normal background changes, so that significant or abnormal changes due to geothermal activity could be recognized. The radiant geothermal heat for the whole area resulted in an estimate of about 2 GW of thermal energy.

Other examples and applications to other areas can be found in some recent literature like Qin et al. (2011) and Eskandari et al. (2015) amongst others.

Most of the aforementioned works used data acquired on specific dates and times, based on their availability. Regarding time series, the use of Landsat and ASTER limited the studies to a temporal frequency of 16 days or more (due to clouds or lack of acquisitions), which might not be sufficient to monitor changing surface conditions. In this context, Vaughan et al. (2012) increased the temporal frequency by using MODIS 1 km radiances. These are typically taken four times daily (twice at day and twice at night).

Night time acquisitions were preferred in all these studies to analyze geothermal anomalies so that sun heating effects were minimized. In particular, at the coldest time of the day (pre-dawn), the relative contribution of the geothermal component to LST is higher. However, with the aforementioned datasets, it was not always possible to choose a specific analysis time and date because of the limitation in acquisition time over a specific area.

Bearing these drawbacks in mind, it seems reasonable to explore the use of geostationary satellites, which provide thermal data at higher temporal frequencies, namely 15, 30 or 60 min. This type of data improves the ability to monitor geothermal areas in a more continuous and consistent manner, as well as facilitates the geothermal research during night acquisition times.

In particular, the present paper aims to explore the use of Meteosat Second Generation (MSG) time series to map geothermal anomalies and calculate the geothermal component of LST (LST_{gt}). The MSG system provides LST products at a temporal resolution of 15 min and a spatial resolution of 3 km at nadir. The satellite is centered at 0° longitude over the equator with a field of view that covers Europe, Africa and the east side of South America. The formulation for LST retrieval is based on a split-window algorithm (Wan and Dozier, 1996) where brightness temperatures and surface spectral emissivity are the inputs.

The spatial resolution of this data is a limitation when aiming to capture geothermal anomalies that are scattered in space and not always detectable with remote sensors. Vaughan et al. (2012) reported that no clear LST anomalies could be observed at the Yellowstone park when using 1 km resolution MODIS LST products, by comparing the central geothermal pixel with the neighboring ones. Bearing this in mind, an alternative strategy was adopted in this research, where instead of using neighboring pixels to analyze the possible thermal anomalies, an additional LST dataset was included and the assessment was carried out comparing both datasets per pixel.

Simulations obtained with the land surface model (LSM) Noah (Niu et al., 2011) implemented in the Weather Research & Forecast (WRF) model were the second dataset. The equivalent to remote sensing LST is skin temperature in the LSM, which is calculated using a single linearized surface energy balance equation. This LSM does not include a source of subsurface geothermal heat in the formulation, and therefore the surface temperature simulated values will be underestimated in geothermal areas. However, remote sensing techniques based on radiation detection are potentially able to detect the whole radiative surface thermal signal. Therefore, the hypothesis here is that the difference between the two datasets is partially related to the geothermal activity.

Different approaches have undertaken a comparative analysis of LST from remote sensing data and modeling approaches with different objectives (Sohrabinia et al., 2012). Some works attempt to improve LST retrievals via modeling complex land cover and terrain features to improve surface emissivity estimation. Others have attempted to use remote sensing thermal and land cover data to improve atmospheric models for simulation of land surface parameters. Others have used remote sensing LST to study the near-surface air temperature or surface soil moisture. Finally, validation of MODIS LST products was carried out using modeling and in situ measurements.

Therefore, bearing in mind that in general the simulated LST could deviate from remote sensing based LST due to differences in inputs (vegetation, elevation, moisture availability, albedo), and model realizations, the objective here was to achieve a major isolation of the geothermal component, in particular for estimating the geothermal contribution to LST (LST_{gt}).

Two approaches of different nature and complexity were developed, adapted and tested to obtain LST_{gt}. In comparison with the aforementioned literature, they take advantage of the high resolution time series and use two LST datasets (a remote sensing based and land surface model outputs). In the first proposed approach, the methodology given by Romaguera et al. (2012, 2014) was adapted for geothermal applications. The aforementioned research was initially conceived as a tool to assess irrigation by comparing remote sensing and model simulations of evapotranspiration. As a human action, irrigation was not included in the simulations whereas its effects were actually observed via remote sensing. A similar concept was adapted in the present paper. The geothermal source of heat was not included in the simulations whereas remote sensing observations were able to capture the radiative part of it. The adapted approach (a bias method, BIASM in the following) was based on the definition of a reference bias, i.e. the difference between the two LST datasets in non-geothermal areas. Clustering of the area was carried out based on hydro-meteorological and surface properties and a spatial mean LST bias was assigned per cluster. LST_{gt} was then calculated in the whole area as the LST difference between remote sensing and simulations corrected by the reference bias.

The second approach (a data mining method, DMM in the following) developed in this paper was based on data mining and used machine learning techniques to train and build a model that predicted remote sensing LST in reference areas (non-geothermal). The inputs for this model were hydro-meteorological and surface properties obtained from the LSM simulations. The hypothesis here was that when applying the model to geothermal areas, remote sensing predicted LST would be underestimated with respect to measured remote sensing LST since model inputs proceed from simulations, which do not account for the geothermal influence. The LST difference between remote sensing measured and predicted LST provided LST_{gt}.

BIASM and DMM were tested in Kenya, in an area of about 560 × 560 km^2 centered at the Kenyan Rift, where numerous geothermal fields are present. This is an area of great geothermal energy potential, where reconnaissance studies have been carried out since 50s and exploitation exists since 80s in specific areas. In particular, the most important power plant is located in the Olkaria field, next to Lake Naivasha. The analysis was carried out in a time span of 45 days in January and February 2012, by using the night time data obtained at 03:00 UTC (pre-dawn in the study area).

The results were tested by comparing the estimates of geothermal area with existing maps of potential geothermal, built based on surface studies. Moreover, the method given by Vaughan et al. (2012) was applied to the Olkaria area and the radiant geothermal flux was compared with the results of this paper.

The general objective of this work is to fill a knowledge gap in the

geothermal field, by using datasets that were not used before and combine them in a manner that was not done before, in order to overcome specific limitations of existing methodologies. Specifically, the objective of this paper is to compare and model the differences between the two LST datasets daily and at a regional scale, by assuming that the discrepancies are partly due to the fact that the geothermal component is only represented in the remote sensed data. This allows determining geothermal areas and comparing the results with the geothermal area map given by Omenda (2010). Moreover, LST_{gt} magnitude might be contrasted with the results obtained using the method of Vaughan et al. (2012). The paper proposes an innovative strategy for geothermal analysis in terms of the developed methods and the datasets used.

The next section of this paper describes the main characteristics of the study area, followed by the datasets. Thereafter the two proposed approaches are explained. The Results section includes the application to the study area and the comparison with existing literature and methods. Section 6 elaborates on the input uncertainties and finally discussion and conclusions of this work are included.

2. Study area

The Kenyan Rift was selected to carry out the present research since geothermal fields are numerous in the area. Rift zones occur when lithospheric plates are thinned by tectonic extension and convection at zones of upwelling hot material. The continued supply of magma to this separation zone increases heat flow and thermal energy at shallow depths compared to other tectonic settings.

The geothermal fields in the East African Rift are characterized by high temperatures (~300 °C) and shallow heat sources (~6 km) and are indicated by geothermal surface manifestations such as fumaroles, steam jets, steaming grounds and solfatara (King and Metcalfe, 2013). Estimated geothermal energy resource potential in the East African Rift is > 15,000 MWe (Teklemariam-Zemedkun, 2011), however only Kenya and Ethiopia have installed a capacity of about 594 and 7 MWe respectively according to the report given by Bertani (2015). Geothermal funding was announced in late 2015 and will motivate further development in these areas.

Reconnaissance studies of geothermal prospects in Kenya started in the 1950s. The most important prospects were mapped by Omenda (2010) and their location is illustrated in Fig. 1. The figure indicates also the extent of the spatial domains used in the present paper. Domain 2 (in green) defines the study area and covers an area of about 560 × 560 km^2 centered at the Kenyan Rift. Domain 1 (in red) was used to initiate the LSM simulations at a coarse scale.

The most explored and developed field in Kenya is the Olkaria geothermal field, where geothermal plants have been producing electricity since the year 1981. There are currently six geothermal power plants operating at Olkaria, some of them having come on line just recently (Olkaria 1 through 4 and Oserian binary and flash). The Oserian plants are smaller, just a few megawatts. Geothermal features at Olkaria were mapped by Clarke et al. (1990) by means of surface studies. The extent of thermal ground in Olkaria was quantified by Hochstein and Kagiri (1997). They provided a value of about 13 km^2 of area with a temperature higher than 30 °C (at 1 m depth). In recent years, remote sensing studies have used high spatial resolution data from airborne thermography and Landsat thermal data for geothermal mapping in this area and others along the Rift (Mutua et al., 2013; Pastor, 2010).

3. Data

The main inputs used in this work are the LST values obtained from the Meteosat Second Generation (MSG) remote sensing data and the LST model simulations. The remote sensing dataset provides a diagnostic value of LST, which means that based on specific states of the surface (emitted radiance and emissivity in this case) an LST value is calculated. However, the data obtained from simulation are prognostic; they use surface and atmosphere states in previous time steps to predict specific parameters to calculate LST. In this paper, the Weather Research & Forecast (WRF) model was used to run the simulations. The implementation of this model is relatively straightforward due to the common use and it incorporates several land surface models which are coupled to atmosphere dynamics.

Hydro-meteorological and surface parameters were also employed by the approaches proposed in this work and were obtained from the simulations.

Additional imagery from ASTER was also used in the region of the Olkaria geothermal field in order to apply the method given by Vaughan et al. (2012) and validate the results at local scale. Table 1 summarizes the specifications of the data sets used in this research.

From a technical point of view, the combination of data with different spatial resolution, extent, and geographical projection was tackled by creating a layer stack where data were resampled (via the nearest neighbor technique) and re-projected to a common output projection. The present work was carried out at the spatial resolution of 3.5 km.

3.1. Period of analysis and time

The study was carried out during the 45-days period between January 1st and February 14th, 2012. The Global Land Data Assimilation System (GLDAS) (Rodell et al., 2004) rain and snow products were used to identify 25 consecutive dry days (16 to 41) in the center of Olkaria geothermal field. These products have a spatial resolution of 0.25° (about 30 km at the equator) and are provided every 3 h. The variables are delivered using different land surface models, from which Noah model was selected.

The analysis time was selected so that the sun heating effects were minimized. During the period of analysis, the sun rose on the east side of the study area between 03:20 and 03:42 UTC (time zone GMT + 3), and about 20 min later on the west side. The pre-dawn timing at 03:00 UTC was selected as a reasonable timing when surface temperatures were close to the minimum in the whole area.

The first 24 h of the analysis were the spin-up time required by the model simulations to reach a balanced state with the boundary conditions. The data from the first day were not used in succeeding calculations.

3.2. Remote sensing data: LST and surface emissivity

The LST products from the Meteosat Second Generation (MSG) satellites (LST_{MSG} in the following) are provided by the Land Surface Analysis Satellite Applications Facility (LSA-SAF, 2010) at a resolution of 3 km at nadir point which increases with the observation angle, and a temporal frequency of 15 min. These data cover the continents of Europe and Africa and partly South-America and are available since February 2009.

The methodology to retrieve LST is based on clear-sky measurements from MSG system in the thermal infrared window following the formulation of a generalized split-window algorithm given by Wan and Dozier (1996). Inputs for this algorithm are brightness temperatures measured in the channels centered at 10.8 and 12.0 μm, and spectral emissivities in these two channels. In particular, average emissivity (ε_{mean}) and the difference between these two channels ($\Delta\varepsilon$) are used.

LST accuracy values, obtained from theoretical and validation exercises, are also provided with the dataset, with values lower than 2 K in the majority of the study area during the period of analysis.

These data sets used the cloud mask from the Nowcasting service (NWC-SAF, 2010) to filter cloudy pixels, which are shown as missing values in the products.

MSG surface spectral emissivity products were generated by LSA-

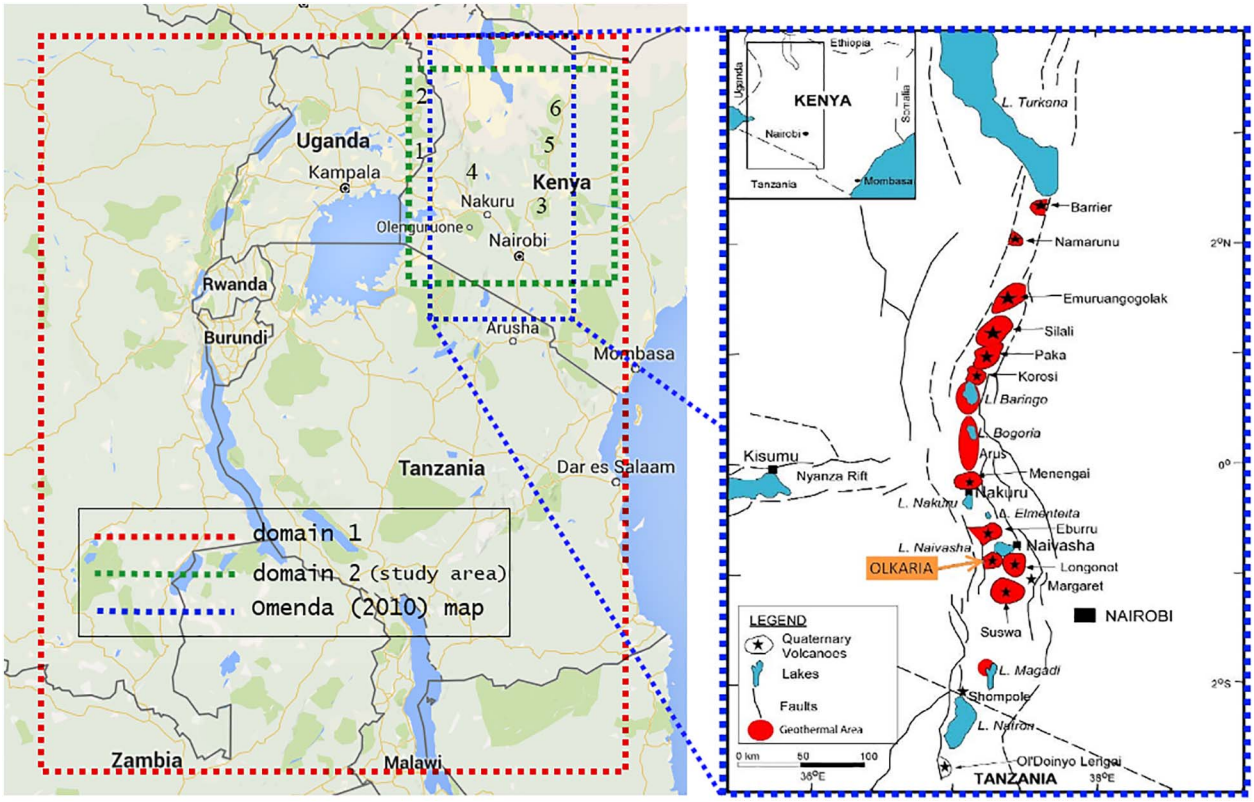

Fig. 1. East African map where working spatial domains are indicated together with the location of geothermal areas given by Omenda (2010). The Olkaria geothermal field is highlighted for its relevance in the present work. Relevant landmarks are labelled as follows: 1) Mount Elgon, 2) Mount Moroto, 3) Mount Kenya, 4) Kerio Valley National Park, 5) Namunyak Wildlife Conservation Trust and 6) Marsabit National Reserve. (For interpretation of the references to color in this figure, the reader is referred to the web version of this article.)

Table 1
Specifications of the datasets used in this paper.

Data	Source	Spatial coverage	Spatial resolution at the study area	Temporal resolution	Details
LST[a]	MSG product	MSG disk[b]	3–4 km	15′	LSA-SAF (2010)
ε_{mean}, $\Delta\varepsilon$	MSG product	MSG disk	3–4 km	Daily	LSA-SAF (2010) Channels 10.8, 12.0 μm
LST, H, λE, G_0, T_{air}, S_{down}, L_{down}, L_{up_TOA},	WRF simulations	East Africa	4 km	1 h	Skamarock et al. (2008) WRF (2012)
$Rain_c$, $Rain_{nc}$				Aggregated from 1 h to daily (previous 24 h)	
ε_s, α_s, h				Static	
LST, ε, Level 1B radiances At-surface radiances	ASTER product	Olkaria geothermal area	90 m	On-demand	Gillespie et al. (1998)

[a] List of acronyms: LST (Land Surface Temperature), MSG (Meteosat Second Generation), LSA-SAF (Land Surface Analysis Satellite Application Facilities), ε_{mean} (mean surface emissivity), H, λE and G_0 (sensible, latent and ground heat flux), T_{air} (air temperature at 2 m), ε_s and Δε (mean surface emissivity and spectral difference), α_s (surface albedo), S_{down} and L_{down} (shortwave and longwave incoming radiation), $Rain_c$ (accumulated total cumulus precipitation), $Rain_{nc}$ (accumulated total grid scale precipitation), L_{up_TOA} (top of atmosphere outgoing long wave), h (terrain height), WRF (Weather Research and Forecasting Model) and ASTER (Advanced Spaceborne Thermal Emission and Reflection Radiometer).

[b] Meteosat disk covers Europe, Africa and part of South America.

SAF (2010) as a function of the (satellite-derived) fraction of vegetation cover (FVC) and land cover classification (Caselles and Sobrino, 1989; Peres and DaCamara, 2005). This product was also generated by the LSA-SAF with the same spatial resolution and coverage as LST, at a temporal frequency of one day.

3.3. Model simulations: LST, hydro-meteorological and surface parameters

The simulated data were generated using the Weather Research and Forecasting (WRF) model with Advanced Research WRF (ARW) version 3.3 (Skamarock et al., 2008; WRF, 2012), hosted at the National Center for Atmospheric Research (NCAR). WRF is a next-generation mesoscale numerical weather prediction system designed to serve both atmospheric research and operational forecasting needs. Fig. 2 illustrates the

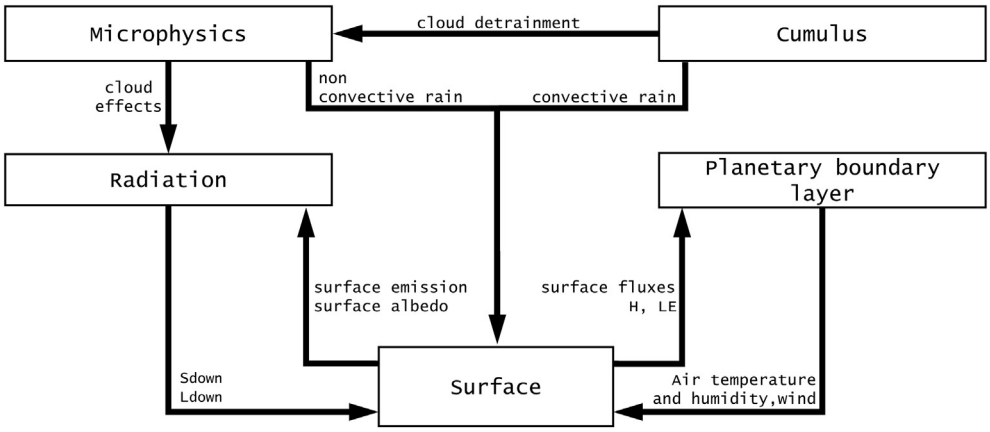

Fig. 2. Direct interactions of parameterizations in WRF.

direct interactions of parameterizations in WRF. The selection of atmospheric schemes was based on the properties of the area, which are WSM 6-class graupel scheme for microphysics option, CAM scheme for longwave and shortwave radiation option and Kain-Fritsch scheme for cumulus option. The reader is referred to the user's guide (WRF, 2012) for detailed information about these schemes. Regarding the land surface physics, WRF includes four coupled land surface models (LSM): five layer thermal diffusion, Noah, RUC, and Pleim-Xiut, which use different formulations for surface energy and moisture balances (Zeng et al., 2015). In particular, Noah model (Niu et al., 2011) in WRF uses remote sensing based land cover categories obtained with MODIS. This aspect resulted very convenient in the current research due to the nature of the study, and therefore Noah model was chosen as the land-surface scheme.

Noah uses four soil vertical layers (of soil temperature, water + ice, water content), at 0–0.1, 0.1–0.4, 0.4–1.0, and 1.0–2.0 m, one vegetation type in each grid cell without dynamic vegetation and carbon budget, and predicts soil moisture and temperature in four layers. A diffusion equation for soil temperature is used to obtain the ground heat budget and the skin temperature is determined using a single linearized surface energy balance equation. Since skin temperature is the simulated parameter equivalent to LST_{MSG}, it will be referred to as LST_{WRF}. This model does not incorporate any source of geothermal heat in the formulation.

Meteorological lateral boundaries and initial conditions for this calculation were taken from the ERA-Interim reanalysis (Dee et al., 2011) and surface properties from land cover maps and remote sensing data like the MODIS land cover map.

The simulation generated values of sensible, latent and ground heat fluxes (H, λE and G_0 respectively), air temperature (T_{air}), shortwave and longwave incoming radiation (S_{down} and L_{down}), accumulated total cumulus precipitation ($Rain_c$), accumulated total grid scale precipitation ($Rain_{nc}$), and top of atmosphere outgoing long wave radiation (L_{up_TOA}) amongst others. Section 4.1.3 elaborates on the criteria to select these parameters.

WRF model was run at a coarse resolution of 20 km, and then by means of a dynamic nesting, results were obtained at a resolution of 4 km. Results were generated in the period between January 1st and February 14th, being the initial 24 h the spin-up time for the model to reach hydrological balance. In the time domain, results were stored every hour. The first spatial domain covered Tanzania, Uganda, Rwanda, Burundi and partly Kenya, Democratic Republic of Congo, Zambia, Malawi and Mozambique as indicated in Fig. 1. The nested domain covered the Kenyan Rift and the surrounding regions.

3.4. Datasets to test the approaches

3.4.1. Geothermal area map

The map given by Omenda (2010), indicates the locations of geothermal areas in the Kenyan Rift (see Fig. 1). Surface studies were carried out to characterize the geothermal prospects in the region. These included geological mapping, seismic, gravity and resistivity measurements, gas thermometry and chemistry, thermal surface manifestations sampling (fumaroles and hot springs) and environmental baseline surveys.

In the present work, this map was digitalised in order to compare the extent of the geothermal areas, bearing in mind that the proposed method is able to capture them only if they are manifested at the surface as an LST increase.

3.4.2. Radiant geothermal flux. ASTER data

ASTER data products were used to apply the method of Vaughan et al. (2012) to calculate the radiant geothermal flux in the Olkaria geothermal area and compare the results with the outputs of the proposed approaches. ASTER data included radiometrically calibrated, geometrically corrected at-sensor radiance (ASTL1B), surface kinetic temperature (AST08), surface emissivity (AST05) and at-surface radiance (AST09T). The ASTER data acquired on 7th January 2012 at 20:09 UTC (23:09 local time) were selected for this analysis.

4. Methods

4.1. Introduction and common steps

The present work is based on the hypothesis that thermal infrared remote sensing is able to capture the radiative part of the geothermal flux in geothermal areas, whereas WRF model simulations lack this component in their formulation, and therefore they underestimate LST.

Fig. 3 exemplifies the differences between the two LST datasets obtained in a geothermal (Olkaria area) and non-geothermal pixel (eastern flat areas), during the period of study. One value per night at 03:00 UTC (06:00 local time) from LST_{MSG} and LST_{WRF} was plotted. LST_{MSG} was systematically higher in the geothermal area during the period of analysis, with typical temperature differences of 5 K.

According to the hypothesis, these differences could be partially due to geothermal influence. The non-geothermal area presented also discrepancies between data sets. These showed lower amplitude and a more fluctuating pattern. A preliminary analysis (not shown here) indicated that these differences were varying from pixel to pixel, thus there was spatial and temporal change.

Reasons for the discrepancies between the two LST datasets (in both geothermal and non-geothermal areas) are generally related to differences in the input parameterizations (vegetation, elevation, soil

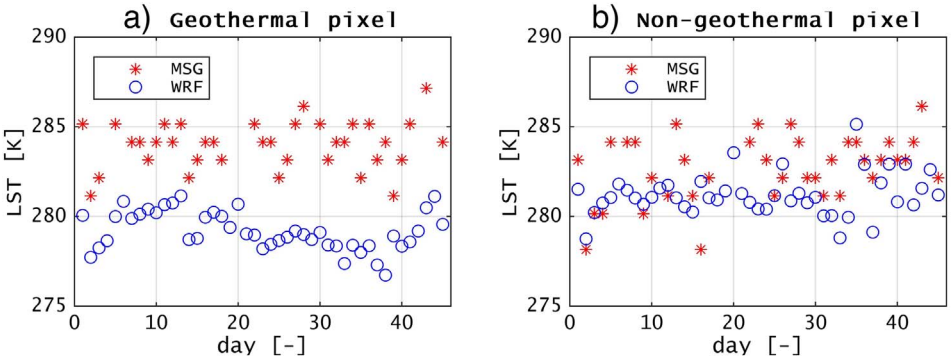

Fig. 3. LST_{MSG} and LST_{WRF} in a) a geothermal pixel at Olkaria field and b) non-geothermal pixel (eastern flat areas in Kenya) during the period of study in the year 2012. (Note: One value per night (03:00 UTC) is plotted in the graphs).

moisture availability, albedo) and model realization. An overview of LST comparative studies can be found in Sohrabinia et al. (2012). Bearing this in mind, the objective here was to achieve a major isolation of the geothermal part, i.e. the geothermal contribution to LST (LST_{gt}).

Two approaches for LST_{gt} estimation of different nature and complexity were developed, applied and compared. The first one (a bias method, BIASM in the following) assessed LST_{gt} by subtracting LST_{MSG} and LST_{WRF} and correcting the results with a LST bias value obtained in reference non-geothermal areas. The second one based on data mining (DMM in the following), built a model to predict LST_{MSG} from hydro-meteorological and surface properties (from simulations) in non-geothermal reference areas. The difference between measured and predicted LST_{MSG} values when applied to geothermal areas resulted in the LST_{gt}. Fig. 4 shows the steps and type of intermediate outputs in both approaches. A dashed gray line surrounds common steps in both approaches (selection of analysis time, definition of reference areas, and selection of hydro-meteorological and surface parameters), which are elaborated in the following. Sections 4.2 and 4.3 detail specific steps of every approach and Section 4.4 includes details of data processing carried out to validate the results with an established method.

4.1.1. Selection of analysis time

Pre-dawn acquisitions were used in order to minimize the sun heating influence. These are the moments where the minimum value of LST is achieved and the relative contribution of LST_{gt} to LST is higher.

During the period of analysis, the sun rose on the east side of the study area between 03:20 and 03:42 UTC (time zone GMT + 3), and about 20 min later on the west side. The pre-dawn timing at 03:00 UTC was selected as a reasonable timing when surface temperatures were close to the minimum in the whole area.

4.1.2. Definition of reference areas

LST datasets from MSG and WRF were used to define reference areas in the study area. No apriori knowledge of the geothermal areas was needed by using this strategy. This is specifically useful in areas where geothermal surveys and exploration are limited and/or not updated in time.

The temporal mean (μ) and standard deviation (σ) of the LST difference MSG-WRF (in the following ΔLST) obtained in the whole period at 03:00 UTC were used as indicators to define geothermal detectability and reference areas.

Two criteria were defined to determine areas with geothermal detectability. The rest of the areas were described as reference areas. The first criteria takes into account the ΔLST temporal mean (μ). Areas with geothermal detectability potential are defined in this paper as areas with sufficient difference between remote sensing and model simulation LST's, so that geothermal anomalies can be detected based on the presented approaches. MSG LST accuracy values from theoretical and validation exercises are provided with the LST dataset and are lower than 2 K in the majority of the study area during the period of analysis. Therefore, a minimum temporal ΔLST mean (μ) of 2 K was selected as a threshold for geothermal detectability.

The second criteria takes into account the ΔLST temporal standard deviation (σ). Differences between data sets might contain transitory fluctuations due for example to differences in reaction time to precipitation events, which might produce false anomalies detection. A maximum temporal ΔLST standard deviation of 1.5 K was selected for filtering these situations. This value was obtained by spatial averaging of σ.

Therefore, areas with potential geothermal detectability satisfy both criteria, the minimum μ and maximum σ, whereas reference areas are the ones that do not meet them.

4.1.3. Selection of hydro-meteorological and surface parameters

Apart from the two LST main datasets, a set of hydro-meteorological and surface parameters was collected. These were needed as inputs of a clustering in the study area (in BIASM) and to build a predictive model in DMM.

Inputs were selected based on three criteria. First, their value must not be influenced by geothermal activity, so that an independent dataset is created. Secondly, the selection of parameters must capture the land-atmosphere interactions and states, and surface properties that might influence the bias between the two temperature datasets in non-geothermal areas. Finally, the parameters must be part of the LST_{MSG} and LST_{WRF} formulations to ensure consistency in the model.

A multilayer file was built per day which contained the following data. From the LST_{MSG} formulation, ε_{mean} and $\Delta\varepsilon$ were selected. These are based on vegetation cover values and a land cover classification that does not incorporate any geothermal feature. MSG brightness temperatures and LST_{MSG} itself were not included since by hypothesis they incorporate implicitly the geothermal component. From the LST_{WRF} retrieval a total of 13 parameters were selected: S_{down}, L_{down} and L_{up_TOA} to account for radiation drivers in the Noah model; α_s, ε_s, LST_{WRF} and T_{air} to account for surface and near-surface properties; H, λE and G_0 to account for land-atmosphere energy exchanges; $Rain_c$ and $Rain_{nc}$ to account for the water balance and *h* to account for topography. Since precipitation changes in short time scales compared to the rest of parameters, an aggregated daily value was calculated using the values during the previous 24 h.

Fig. 5 shows an example of the aforementioned set of 15 parameters obtained on January 7th, 2012 at 03:00 UTC. Cloudy pixels and lakes are masked in white color. Particular surface features can be observed from the dataset, like high mountains (reflected in the height (h) and inversely proportional in T_{air} images). Mount Kenya on the right of the Kenyan Rift and Mount Elgon at the left border of the image can be identified. Rift faults are also recognized, where elevation changes rapidly and the terrain is more complex. Precipitation ($Rain_c$ and $Rain_{nc}$) occurred in the previous 24 h in the southern parts of the Rift, with local values up to 4 mm/day. Most of the area presents negative sensible heat values (H), which indicates that the heat flows from the surface upwards to the atmosphere at this time. Differences between ε_s and ε_{mean} were found in patterns as well as in absolute values.

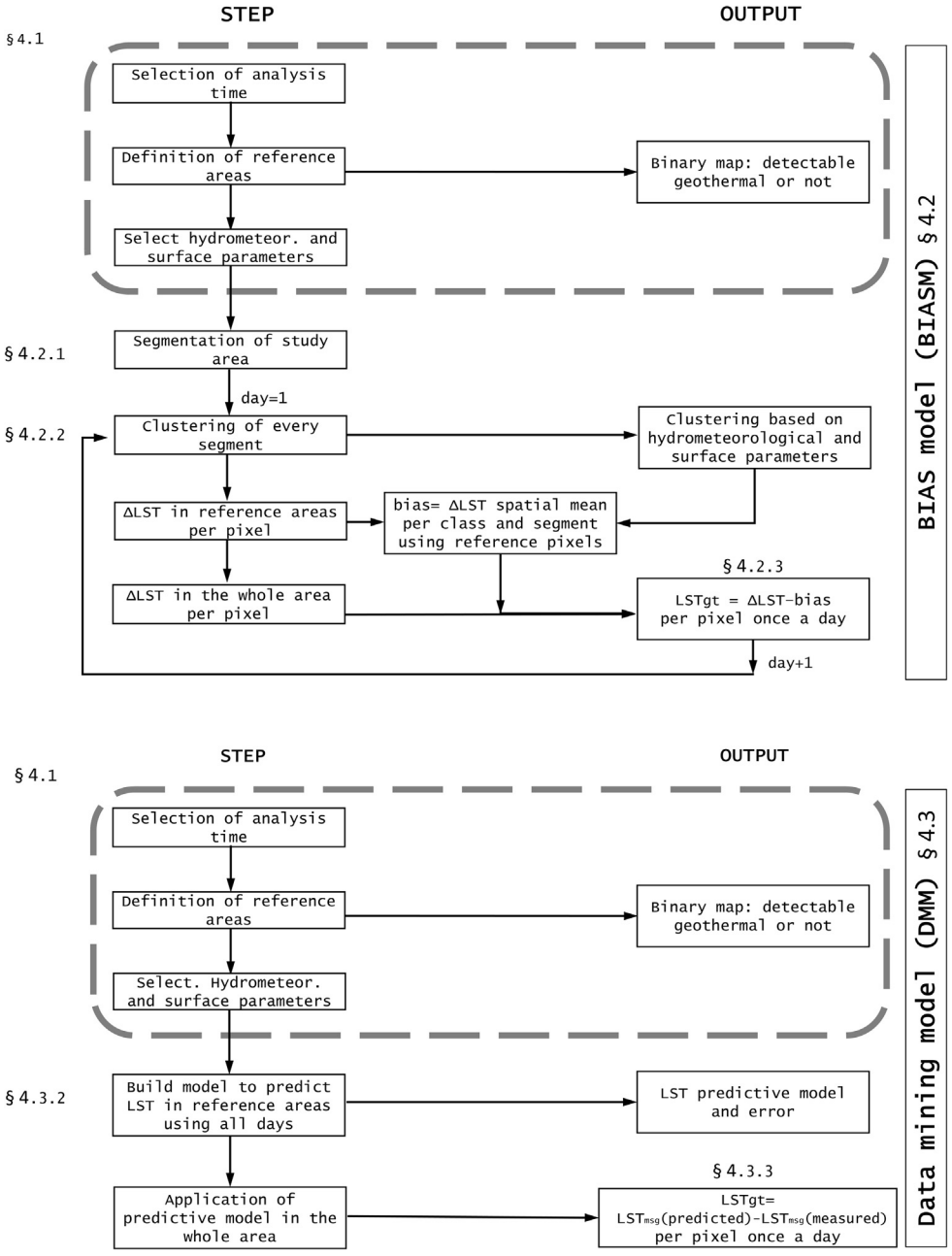

Fig. 4. Schemes of the two approaches proposed in this paper to calculate LST_{gt}. The dashed gray line surrounds common steps in both approaches.

Broadband emissivity is used in WRF (ε_s), whereas the spectral average in bands centered at 10.8 μm and 12.0 μm is used in the remote sensing data. This might explain the differences partially. Moreover, the WRF emissivity values are static, whereas MSG emissivity products are calculated daily from observed fraction of vegetation cover. $\Delta\varepsilon$ patterns are similar to the ones obtained in ε_{mean}. Finally, L_{down}, T_{air}, h, L_{up_TOA} and LST_{WRF} show a similar pattern, as expected due to the physical relationships between them.

4.2. Bias model (BIASM)

The first approach was inspired by the method given by Romaguera et al. (2012, 2014), adapted here to geothermal activity. The aforementioned research was initially conceived as a tool to assess irrigation by comparing remote sensing and model simulations of evapotranspiration. As a human action, irrigation was not included in the simulations whereas its effects were actually observed via remote sensing. A similar concept was adapted in the present paper. The geothermal source of heat was not included in the simulations whereas remote sensing observations were able to capture the radiative part of it. The proposed approach obtains LST_{gt} per pixel as the difference between LST_{MSG} and LST_{WRF} and a LST bias correction according to:

$$LST_{gt} = \Delta LST - bias_{LST} \quad (1)$$

where ΔLST is the difference between LST_{MSG} and LST_{WRF} calculated at the optimal night time and $bias_{LST}$ is the spatial mean value of ΔLST calculated in reference areas (non-geothermal) of similar conditions. Section 4.1.1 elaborates on the selection of the optimal time, which for this paper is 03:00 UTC.

Due to the size of the study area and the spatial variability of surface and hydro-meteorological parameters, this paper recommended an initial segmentation of the study area followed by a clustering (per day) of every segment. This allowed the separation of areas with different surface and hydro-meteorological properties, for which $bias_{LST}$ were obtained separately. These steps are elaborated in the following sections.

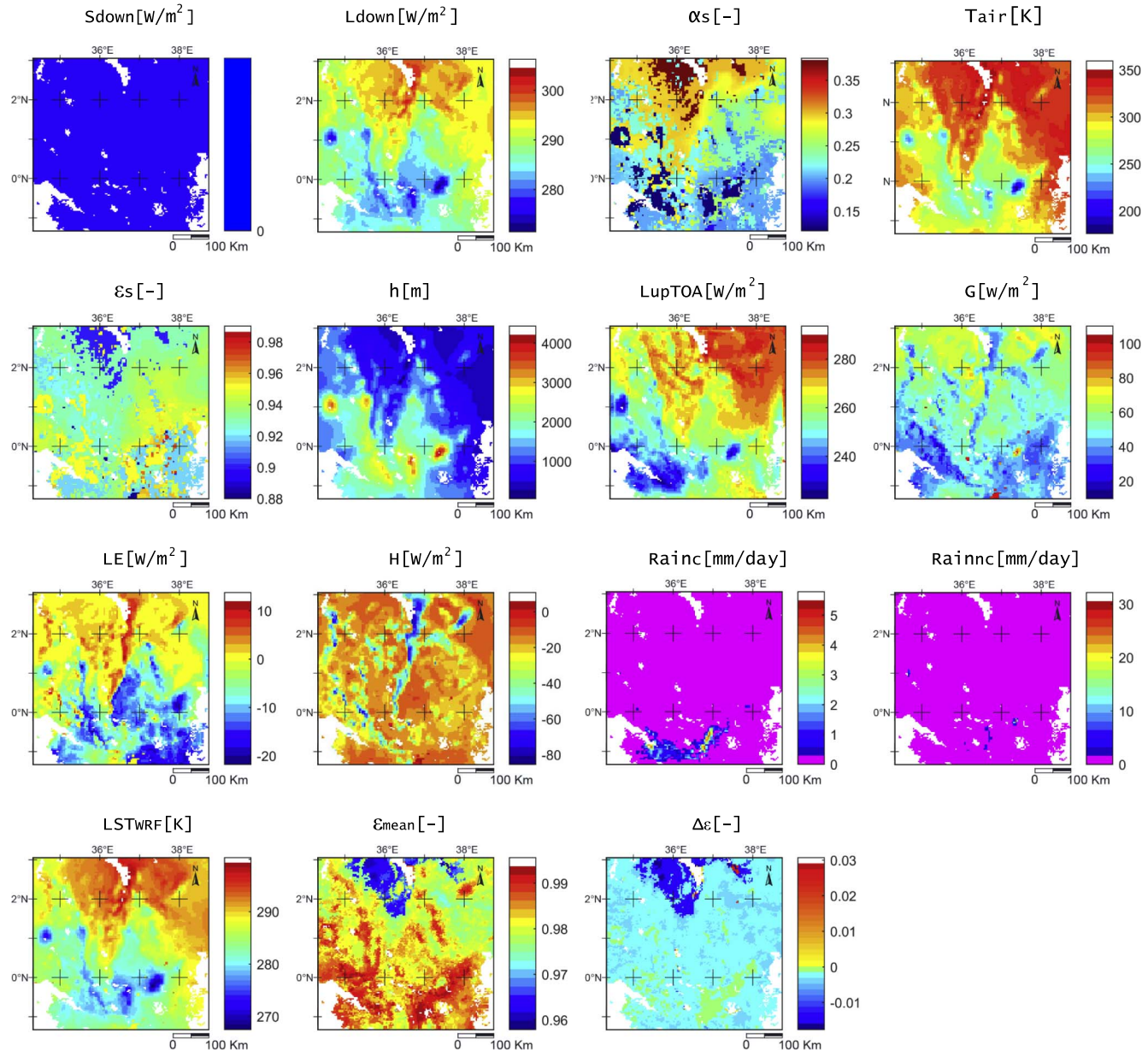

Fig. 5. Set of input parameters (hydro-meteorological and surface properties) for clustering the study area (BIASM) and to build a model to predict LST_{MSG} (DMM) obtained on January 7th, 2012 at 03:00 UTC. Lakes and cloudy pixels are masked in white color.

4.2.1. Segmentation of study area

An initial segmentation of the study area is proposed in the present paper so that biases are obtained independently for smaller regions. The number and size of these depend on the extent and spatial variability in the area. In this paper the study area was divided into square segments of 60 × 60 km^2, computing a total of 8 × 8 segments. This segment area covered a window of about 3 × 3 times the size of an average geothermal area in the region and captured the variability in elevation present in the area, especially in the Rift.

4.2.2. Clustering

Unsupervised clustering based on the k-means statistical technique (Tou and Gonzalez, 1974) was carried out in every segment per day using the multilayer file described in Section 4.1.3 so that pixels with similar properties were grouped. This method calculates initial mass means evenly distributed in the data space and then iteratively clusters the pixels into the nearest cluster using a minimum distance technique. In each iteration, clusters' means are recalculated and pixels are reclustered with respect to the new means. All pixels are clustered to the nearest cluster unless a standard deviation or distance threshold is specified, in which case some pixels may be unclustered if they do not meet the selected criteria. This process continues until the number of pixels in each cluster changes by less than the selected pixel change threshold or the maximum number of iterations is reached.

The 15-layer input file contained the parameters indicated in Section 4.1.3, a maximum of 100 iterations was fixed to ensure completion of the k-means algorithm and the default values of 5% and 5 were conserved for the pixel change threshold and number of clusters (Exelis, 2013). Neither standard deviation nor distance thresholds were fixed.

The k-means approach showed to be sufficient to capture the variability of the bias between two models in the specific application showed by Romaguera et al. (2014), where different clustering methods were investigated.

4.2.3. $bias_{LST}$ and LST_{gt}

For every segment, ΔLST was calculated in pixels of reference areas and their values were spatially averaged per cluster, obtaining $bias_{LST}$. LST_{gt} of a specific pixel in a segment was obtained using Eq. (1) with the $bias_{LST}$ of the corresponding pixel cluster.

In this approach, LST_{gt} was obtained once a day. LST_{gt} time series were obtained by iteration of the described process every day during the study period.

4.3. Data mining model (DMM)

The second approach to estimate LST_{gt} used reference areas to train and build a data-driven model that predicted remote sensing LST_{MSG} from simulated hydro-meteorological and surface properties. The inputs are described in Section 4.1.3 and they are independent of the geothermal activity because they proceed from WRF model simulations. Therefore, when applied in geothermal regions, predicted LST_{MSG} was expected to be lower than the measured LST_{MSG}. The difference of these, corrected by the model error provides LST_{gt} per pixel as:

$$LST_{gt} = LST_{MSG}(\text{measured}) - LST_{MSG}(\text{predicted}) - \text{error} \quad (2)$$

where *error* is the model error.

Various predictive techniques were tested and the best performer was used to predict LST_{MSG} in the whole of the study area.

4.3.1. Techniques

Machine learning techniques were used to build a predictive model valid for the whole period of study. Four algorithms of different basis and complexity were tested: a regularized linear regression (RLR), a decision tree (DTM), a neural network (NN) and a support vector regression (SVR).

The algorithm RLR (Bishop, 2007) performs regularized linear regressions to prevent the overfitting of the inputs to predict LST_{MSG}. The DTM (Quinlan, 1993) is a simple and non-parametric technique that consists of a sequence of branching operations based on decision rules of input values, resulting in the LST_{MSG} predicted values. The NN (Duda et al., 1998; Haykin, 1999) consists of a set of interconnected neurons organized in layers. The signal is propagated from input to output nodes by means of certain weights. Specifically, the Multilayer Perceptron (MLP) was used in this work. Finally, SVR is a statistical learning algorithm based on kernel methods. SVR (Vapnik, 1998) finds a function with a maximum deviation covering the maximum number of targets from all the training data. More detailed information about different types of machine learning techniques can be found in Hastie et al. (2009).

4.3.2. Building predictive model

The predictive model was built using data from the whole study period at the selected study time (03:00 UTC) in reference areas. This allows the model to be trained with a high variety of conditions, which makes it valid for a broader range of values. The input parameters are described in Section 4.1.3.

The input dataset in reference areas was split in two in order to train and test the models. The percentage for training was 20% for the RLR, DTM and NN, and only 1% for the SVR due to computing limitations. The other 80% and 99% was used to test the models respectively. These inputs included all cloud free data from the reference areas at 03:00 UTC during 44 days. Note that the first-day data was discarded since it is the spin-up time required by WRF to reach balance. The number of instances used for training was 95,139 in the three first models and 4,756 in SVR.

For RLR, NN and SVR models, all the parameters were optimized by 5-fold cross validation. The regularized parameter, in RLR, was tuned between (0, 1) in steps of 0.02. The best architecture for the NN model was selected between (2,30) hidden neurons. The SVR was trained with a Gaussian kernel. The bandwidth of the kernel was tuned taking into account the trained data and C (SVR error parameter) were tuned between (1,1000). All the models were generated by SimpleR Matlab toolbox (Camps-Valls et al., 2006). The error of the models was evaluated based on their performance in the test dataset. The selected indicators were the mean error (*ME*), root mean squared error (RMSE), and the correlation coefficient *r*.

4.3.3. LST_{gt}

After generating the predictive model using the different algorithms and evaluating the errors, the best performer was applied to all pixels and the LST_{gt} value was obtained per pixel following Eq. (2).

4.4. Comparison with established method

The method given by Vaughan et al. (2012) to estimate radiant geothermal flux was applied to the region of Olkaria. Since the present work provides results in terms of temperature (LST_{gt}), the associated radiant geothermal flux was calculated for consistency in the comparison.

Under the assumption that remote sensing LST_{MSG} contains a geothermal (LST_{gt}) and a non-geothermal (LST_{nogt}) contributions, the radiant geothermal emittance M (LST_{gt}) (or flux in W/m^2) was calculated by using the Stephan-Boltzmann equation according to the following formulations:

$$\begin{aligned} LST_{MSG} &= LST_{nogt} + LST_{gt} \\ M(LST_{MSG}) &= M(LST_{nogt}) + M(LST_{gt}) \\ M(LST_{gt}) &= M(LST_{MSG}) - M(LST_{nogt}) \\ &= \sigma\,\varepsilon\,(LST_{MSG})^4 - \sigma\,\varepsilon\,(LST_{MSG} - LST_{gt})^4 \end{aligned} \quad (3)$$

where $M(LST_i)$ are emittances (W/m^2) associated to every LST, σ is the Stephan-Boltzmann constant ($\sigma = 5.67036713 \times 10^{-8}\ W\,m^{-2}\,K^{-4}$) and ε is the broadband surface emissivity (taken from the WRF inputs).

5. Results

5.1. Definition of reference areas

Fig. 6 shows the spatial distribution of the indicators selected to define areas with geothermal detectability (and reference areas), namely temporal mean and standard deviation of ΔLST. As a reference, the contours of the geothermal areas reported by Omenda (2010) in Fig. 1 are also included.

ΔLST mean values were distributed mainly in the range −5 K to 5 K. Values higher than 10 K (LST_{MSG} significantly higher than LST_{WRF}) were observed in specific areas corresponding to Lake Victoria (southwest). Lower values were observed in Mount Elgon National Park (middle west) and the city of Nairobi (southeast).

Most of the study area presented a standard deviation lower than 2 K, specifically below 1.5 K in most of the Kenyan Rift. Peaks in standard deviation were observed in the region of Mount Moroto (northwest, see Fig. 1 for reference), Mount Elgon (mid-west), in vegetated areas next to Olenguruone and Kerio Valley National Park (mid-west), Mount Kenya (mid-east), Namunyak Wildlife Conservation Trust, Marsabit National Reserve and bare regions at the northeast of the study area.

In this paper areas with geothermal detectability potential were defined when the temporal mean of Δ_{LST} was higher than 2 K and the standard deviation was below a threshold of 1.5 K. The remaining regions where the aforementioned criteria for geothermal detectability were not met, were defined as reference areas. The resulting binary map is also shown in Fig. 6, where detectable geothermal and reference areas are indicated in white and black respectively.

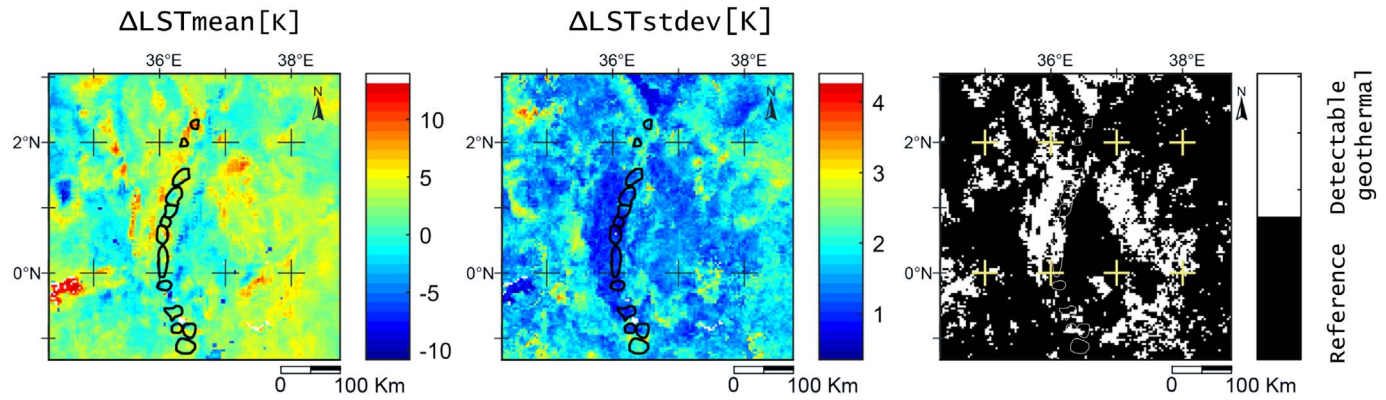

Fig. 6. ΔLST temporal mean and standard deviation during the period of study, and binary map of detectable geothermal and reference areas.

5.2. BIASM: clustering and reference $bias_{LST}$

A clustering was obtained per segment and per day. For every segment, the $bias_{LST}$ was obtained in reference areas per pixel as the difference between LST_{MSG} and $LST_{WRF,}$ averaged per cluster number.

Fig. 7a includes the clustering results per day at 03:00 UTC in the segment of Olkaria. The image shows in black color Lake Naivasha and pixels with no data (e.g. due to clouds). The classification patterns coincided almost 100% in clear sky days and were highly influenced by L_{down}, T_{air}, h, L_{up_TOA} and LST_{WRF}, whereas the influence of other parameters appeared to be less significant. In days with patchy clouds like days 3, 6, 10, 17, 39 or 42, the cluster patterns changed slightly. Finally, classification in days 11 and 18 was very limited due to the number of available pixels.

Fig. 7b shows the variability in time of the $bias_{LST}$ in that segment, with values between −2 and 4 K for the majority of the days of analysis. Moreover, for every day the clustering allows discriminating areas with different $bias_{LST}$ values, i.e. its spatial variability, which ranges between 1 and 4 K. Examples of high $bias_{LST}$ scatter were found in days 35 and 41, which presented significant differences between clusters, being negative in day 35 and positive on day 41. Both days had the same cluster pattern, however, the LST inputs influenced the $bias_{LST}$. Examples of lower $bias_{LST}$ scatter are days 7, 11 and 18, from where the last two were highly influenced by clouds and the biases were calculated using fewer reference area pixels. Therefore, the inaccuracies on these dates are expected to be higher.

LST_{gt} was obtained per day and per pixel following Eq. (1) using the spatial averaged $bias_{LST}$ values per cluster and per segment. To evaluate the performance of the approach in the whole study area, a single value was obtained from the time series. The confidence intervals of 5% and 95% were calculated based on the corresponding values of the 2.5% and 97.5 quantiles. This ensured that 95% of the data set per pixel was contained inside this interval. This is a common approach for identifying outliers. A mean value was recalculated using only the values that fell into this confidence interval and was mapped in Fig. 8. The contour of the geothermal areas reported by Omenda (2010) is also included as a reference. Note that the method produced some negative LST_{gt} values in the series, which were not used in the averaging process described above. These cases occurred when remote sensing LST's were lower than modelled LST's, after correcting for the bias (see Eq. (1)). Since remote sensing was not able to detect geothermal signal in these cases, based on the main hypothesis of this work, they were labelled as 'non detectable geothermal' (or 'non geothermal') and their value was not used for the series LST_{gt} average. Section 5.6 of this paper includes an assessment of the negative LST_{gt} values found in the results, the amount, distribution and implications on the results.

The figure showed LST_{gt} values lower than 2 K in most of the study area, and local LST_{gt} maxima higher than 5 K in specific regions. The approach detected also non-geothermal pixels. These are the cases where LST_{gt} is lower than zero. This means that the value of remote sensing LST_{MSG} (after the $bias_{LST}$ correction) was not sufficiently higher than the simulations, or it was lower. In that case, geothermal activity is not detected with the proposed approach.

Low LST_{gt} values (0 to 2 K) were located in known non-geothermal regions of the country. These might be related to the uncertainties of the LST inputs used in this paper. Section 6 of this paper elaborates on

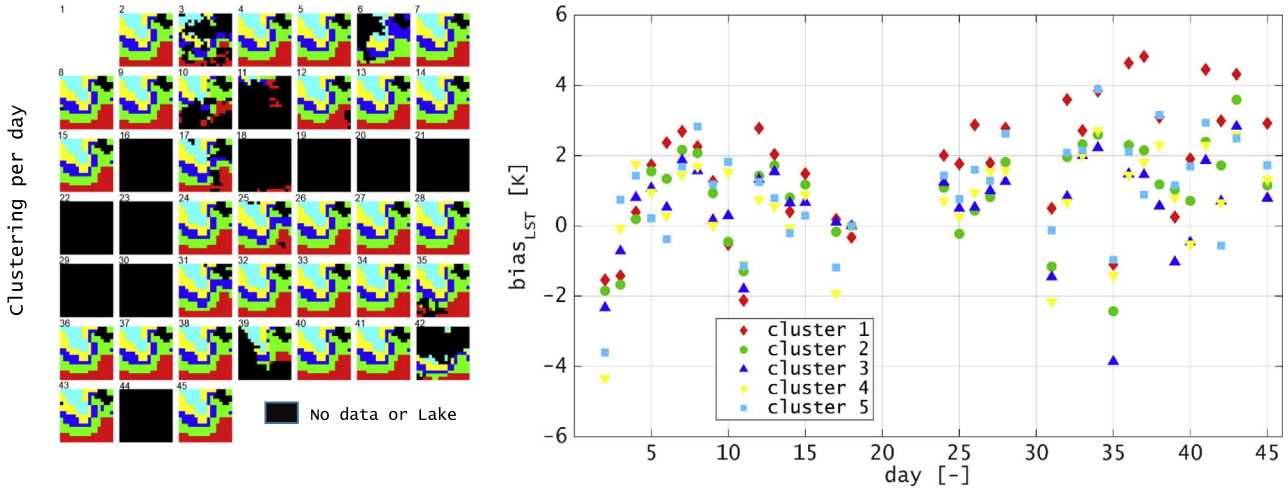

Fig. 7. (a) Clustering results per day during the study period in the segment of Olkaria. (b) $bias_{LST}$ value obtained daily per cluster in reference areas in the segment of Olkaria at 03:00 UTC. Clusters correspond to the areas indicated in (a).

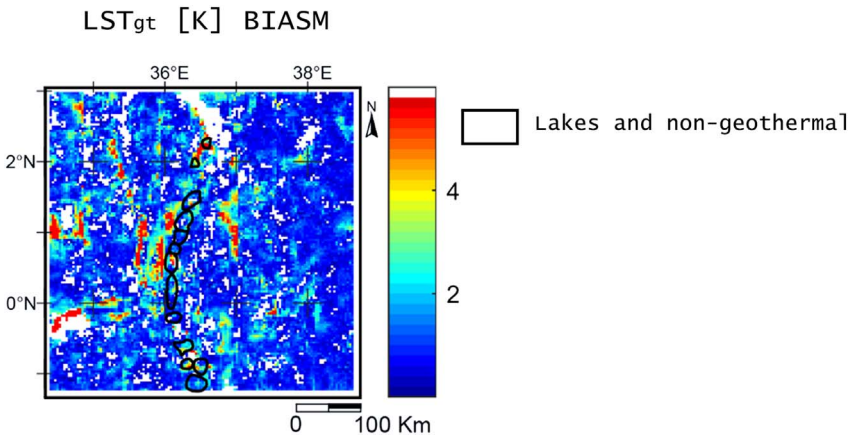

Fig. 8. LST_{gt} averaged in time for the period of analysis, obtained with BIASM. The value was obtained using positive values that fell into the confidence interval between 5 and 95%. Black lines indicate the contours of geothermal areas reported by Omenda (2010). (For interpretation of the references to color in this figure, the reader is referred to the web version of this article.)

this aspect.

The analysis of the peaks was carried out in two manners. First, the map from Omenda (2010) was used to evaluate the performance of the proposed approach in detecting reported geothermal areas in a qualitative manner.

The results showed local maxima in 70% of the 13 areas mapped by Omenda (2010). In the areas of Barrier, Emuruangogolak, Lake Baringo, Olkaria and Longonot, LST_{gt} reached values up to 5 K and more. In lower magnitude, local maxima were found in Lake Bogoria, Arus, Eburru and Suswa up to 2 to 3 K of LST_{gt}. The area covered by the local maxima in Sisali, Paka, Korsi and Menengai was smaller and less discernable. This could be due to modeling issues but also to the inability to detect surface thermal manifestations that may be too small in extent and/or not enough powerful to be detected at the resolution of this study. Moreover, the proposed approach was developed to capture exclusively the geothermal areas with thermal effect on the land surface. Therefore, the map from Omenda (2010) has to be seen as an outer boundary where thermally active but also blind geothermal areas might exist.

Other peaks were false positives and are not associated with the geothermal activity. These were found in Fig. 8 in complex terrain areas with high slope values, where elevation changes rapidly within few pixels, namely from five hundred to thousand meters (see also Fig. 5, for height information). The maxima coincided with the location of the Rift faults (see Fig. 1), Mount Kenya (5100 m elevation) and Mount Elgon (4300 m elevation).

The quantitative analysis of the LST_{gt} values obtained with BIASM and DMM is included in Section 5.4 of this paper.

5.3. DMM: Prediction of LST_{MSG}

The error of the predictive models was evaluated based on their performance in the test dataset. The statistical outputs of the model's test are summarized in Table 2, which informs about the goodness of fit of the models generated. The selected indicators are the mean error (ME), root mean squared error (RMSE), and the correlation coefficient *r*. The values obtained in training specify the best possible fit of the models. The values in test indicate the error of the models.

Based on their performance, DTM model was selected for further calculations of LST_{gt}. This model has a mean error value closer to zero, a lower RMSE value and higher correlation coefficient. Additionally, it is methodologically less complex than NN or SVR and is simple to understand and interpret.

LST_{gt} was calculated by applying the predictive DTM to the whole dataset. Similarly to Section 5.2, Fig. 9 illustrates the temporal mean LST_{gt} value. The contour of the geothermal areas reported by Omenda (2010) is also included as a reference.

In general, the patterns and relative maxima captured by the two approaches were consistent with each other, being BIASM the one that captures a more extensive area with LST_{gt} values about 2 K higher than DMM. Low LST_{gt} (0 to 2 K) in non-geothermal areas were associated to inaccuracies of the inputs, and negative LST_{gt} values to non-geothermal pixels. BIASM and DMM disagree locally in mount Marsabit (1700 m elevation) at the east side of the Rift, where DMM captured a false geothermal anomaly. Other common false positives were found in fault areas as well as in high mountains, as indicated in Section 5.2. The effectivity to map non-geothermal pixels was higher in DMM since the approach produced negative LST_{gt} values in a wider area.

Regarding the comparison of individual geothermal areas, results were similar to the ones obtained in BIASM, being the more evident and powerful anomalies in Emuruangogolak, Lake Baringo, Olkaria, Longonot, Suswa with LST_{gt} values in the range from 3 to 5 K.

Table 2
Statistical data of predictive models where *N* is number of samples and *ME* is the mean error.

		RLR	DTM	NN	SVR
N	Training	95,139			4,757
	Test	380,558			470,940
ME [K]	Training	0.0000	0.0000	0.0053	-0.0243
	Test	-0.0074	**0.0004**	-0.0019	-0.0185
RMSE [K]	Training	2.5267	1.9583	2.2139	2.3933
	Test	2.5270	**2.1627**	2.2172	2.4536
r	Training	0.9073	0.9454	0.9297	0.9178
	Test	0.9067	**0.9327**	0.9290	0.9126

5.4. LST_{gt} values inside and outside geothermal boundaries

For BIASM (Fig. 8), the LST_{gt} average value within the geothermal boundaries reported by Omenda (2010) (Fig. 1) was 1.7 K, compared with the average obtained in the outer region which had a value of 1.2 K. For DMM (Fig. 9), the mean value was 0.8 K, and 0.7 K when calculating it outside the geothermal borders. These values are a first indicator of the goodness of the results, since the average magnitude obtained in the geothermal regions is higher than the obtained in the rest of the area.

Additionally, Fig. 10 plots the histogram of LST_{gt} frequencies normalized with respect to the sample size. The number of valid pixels within the geothermal boundaries is 389 and the number in the outer area is 17,227 in BIASM, and 18,040 in DMM. This normalization allows to analyze the results in terms of relative frequency.

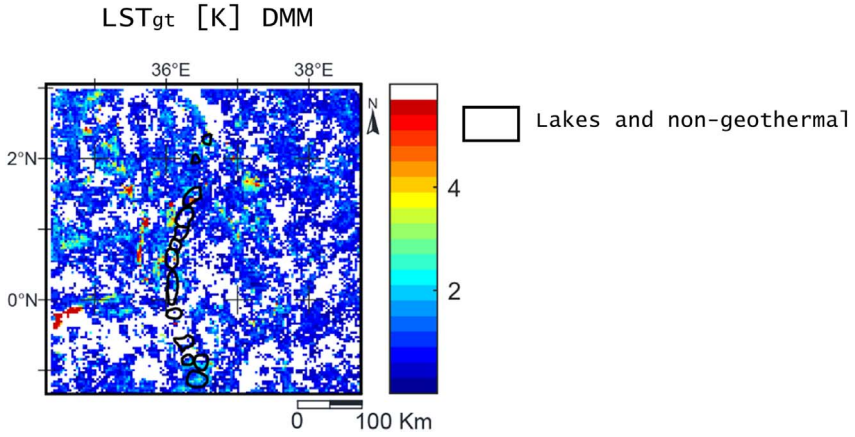

Fig. 9. LST_{gt} averaged in time for the period of analysis, obtained with DMM. The value was obtained using positive values that fell into the confidence interval between 5 and 95%. Black lines indicate the contours of geothermal areas reported by Omenda (2010). (For interpretation of the references to color in this figure, the reader is referred to the web version of this article.)

The normalized histogram indicates that in general, the relative frequency of occurrence is higher inside the geothermal boundaries when LST_{gt} values are higher than 1 K in BIASM and 1.5 K in DMM. This is especially relevant when LST_{gt} values achieve values of 3, 4, 5 K and higher, since it indicates a higher proportion of geothermally detected pixels within the geothermal area.

For lower LST_{gt} values, the histogram of pixels outside the contours presents higher values in both models. This is consistent with the fact that lower LST_{gt} values are associated in this paper to non-geothermal areas. However, a relative high presence of low LST_{gt} values is observed inside the geothermal boundaries, fact that could be associated to inaccuracies of the reference map, but also to data and methodological limitations.

5.5. LST_{gt} time series

LST_{gt} results were obtained on a daily basis per pixel using both approaches. Fig. 11 illustrates the results in the central pixel of the Olkaria geothermal field. Precipitation, as a sum of $Rain_c$ and $Rain_{nc}$ in the previous 24 h is also plotted as a reference. The figure shows that BIASM provides systematically higher LST_{gt} than DMM, in most of the cases with differences below 3 K. Higher differences are achieved in days 2, 12, 26, 31, 35, 38. The values in days 2, 31, and 35 obtained with BIASM are highly influenced by the low negative $bias_{LST}$ values obtained in those days (see Fig. 7). Moreover, the approaches also provide some negative LST_{gt} which are labelled in this work as 'non detectable geothermal' or 'non geothermal'. On day 12, the negative value corresponds to a locally high value of precipitation (accumulated in the previous 24 h), which indicates the possible influence of this parameter in the sensitivity of the models. Finally, the second part of the study period provides slightly higher values in both approaches, also in coincidence with a dry period. Note that LST_{gt} could not be evaluated in some days due to missing input data.

5.6. Assessment of LST_{gt} negative values

Fig. 12 shows the number of days with non-processed data (filtered by clouds, lakes or because of missing input variables), as well as the number of days with negative and positive LST_{gt}. Moreover, the ratio (in %) between the absolute value of the negative temporal mean and the positive temporal mean is included. These four indicators were obtained from BIASM.

Fig. 12a shows the number of days with non-processed LST_{gt}, from where the location of water bodies can be easily identified (100% of days with no processed data). In most of the study area, the number of days discarded for this reason was lower than 15 (out of 44), quantity that increased up to 30 in southern areas at East, West and center and other local areas in the North. Pixels with values above 30 were influenced by nearby water bodies during the calculations and the scaling process.

Regarding the number of days with negative LST_{gt}, Fig. 12b shows the existence of areas where the whole time series presented positive LST_{gt} valid data, and therefore no data were discarded in the temporal mean calculations. Peaks in LST_{gt} identified in Figs. 8 and 9 coincide with these areas. The total number of negative data in the rest of the study area varies per pixel, with values from few days to the whole time

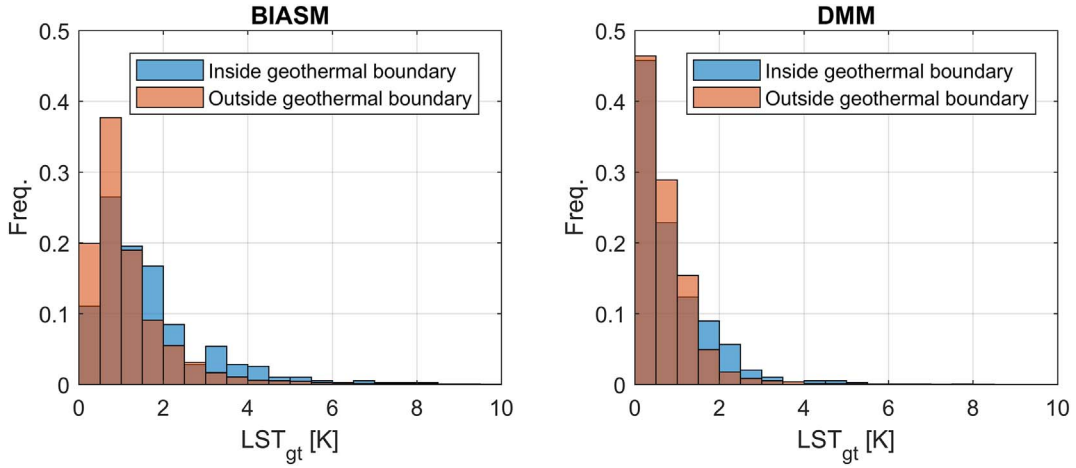

Fig. 10. Histogram of LST_{gt} frequencies normalized with respect to the sample size, where the first sample contains the pixels within the geothermal boundaries of Omenda (2010) and the second sample the rest.

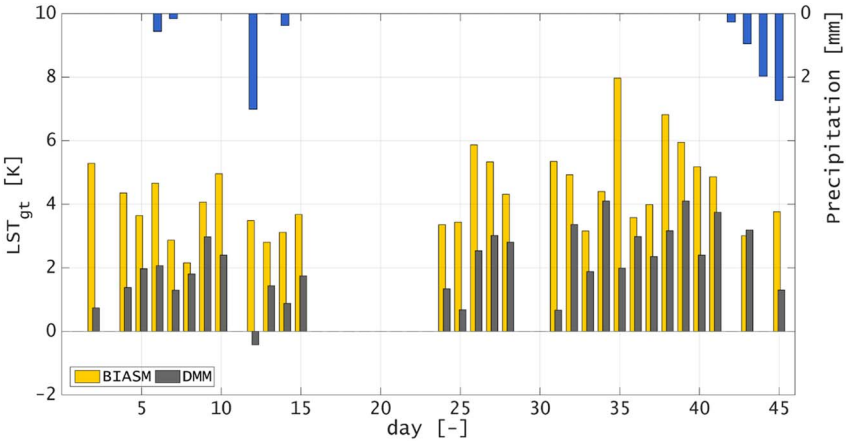

Fig. 11. LST_{gt} obtained per day at 03:00 UTC with the two approaches proposed in this paper during the period of analysis in Olkaria geothermal field pixel. Precipitation as the sum of $Rain_c$ and $Rain_{nc}$ accumulated in the previous 24 h is plotted on the additional Y axis. (central coordinates of the pixel 0°52′49.98″S, 36°17′29.21″E).

series. In this paper, negative values were related by hypothesis to non-geothermal or (non geothermal detectable) pixels. These cases occurred when remote sensing LST's were not sufficiently higher than model simulations. Therefore, the negative values were not used in the temporal mean of Fig. 8, but considered as non-geothermal.

Fig. 12c shows the number of positive LST_{gt} used in the temporal mean calculations in Fig. 8. This map is in general complementary to Fig. 12b and both could be used as indicators of the reliability of the results, and could suggest the need of a more extensive time series analysis. Moreover, Fig. 12d shows the ratio between the negative and positive temporal means of LST_{gt}. An inverse relationship between this ratio and the number of valid days in Fig. 12c was observed. Most of the Kenyan Rift presented values below 25%, however an extensive area showed values up to 100% and above. In the latter case, the magnitude of this ratio is linked to the non-geothermal character of the pixels.

The results obtained from DMM (not shown here) presented a substantial increase in the number of days with negative LST_{gt} in the study area, a decrease of positive days, and a ratio pattern similar to Fig. 9, where non-geothermal areas (in white) were pixels with low ratio.

5.7. Assessment of vegetation definition implications

The effect of land cover and vegetation in the approaches presented

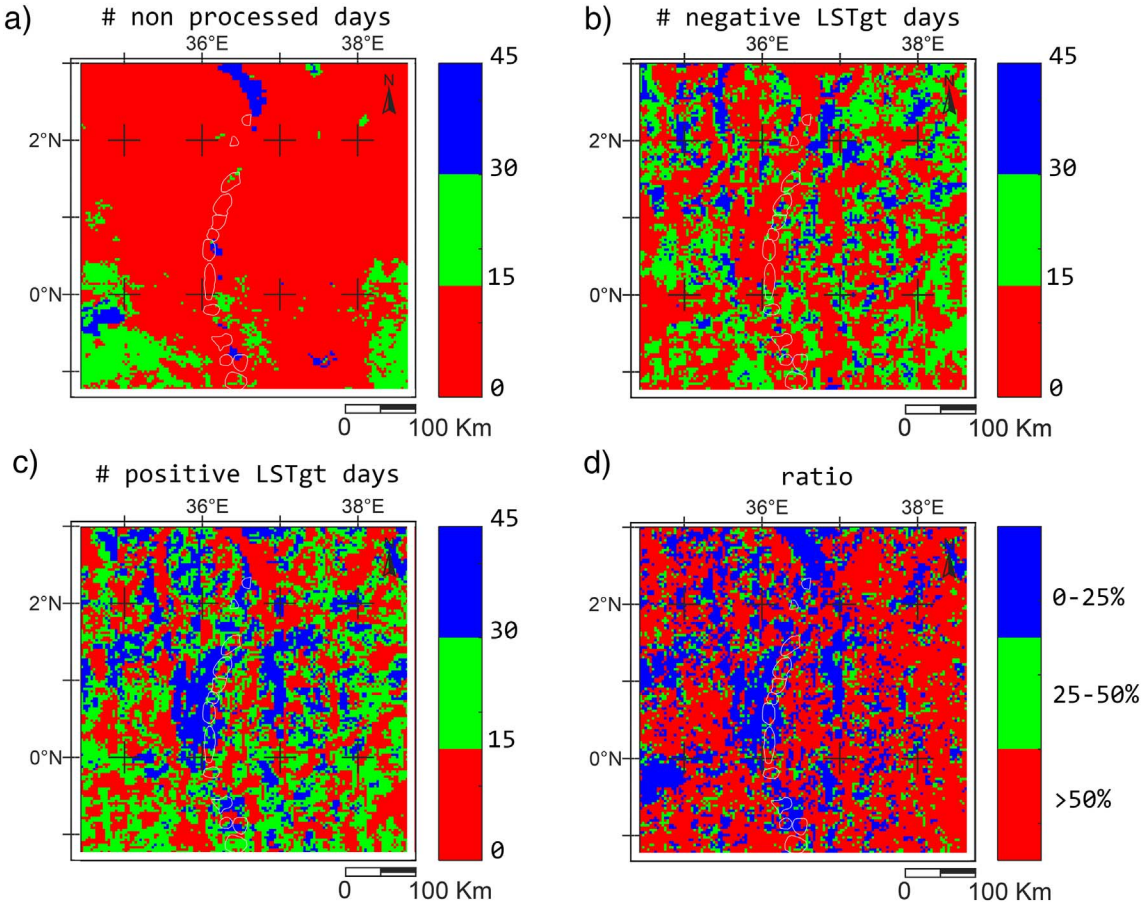

Fig. 12. a) Number of days with non-processed data, b) number of days with negative LST_{gt}, c) number of days with positive LST_{gt} and d) absolute value of the negative temporal mean divided by the positive temporal mean LST_{gt}s, obtained using BIASM (in %). Note that the total number of used days is 44.

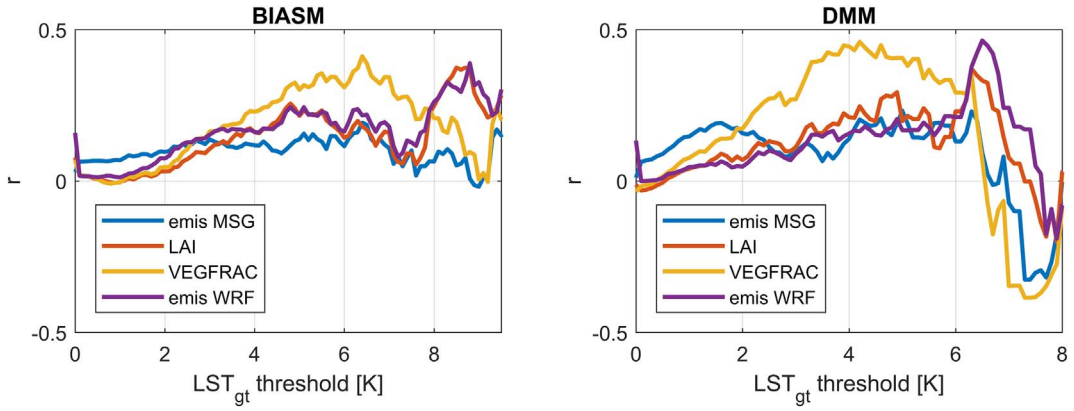

Fig. 13. Pearson's correlation coefficient (r) between temporal mean LST_{gt} and vegetation parameters, where r is calculated using pixels with LST_{gt} above the indicated threshold. Note that ε_{mean} and ε_s have been named in the figure 'emis MSG' and 'emis WRF' respectively.

was taken into account by selecting relevant parameters in the input dataset as elaborated in Section 4.1.3, namely ε_{mean} and $\Delta\varepsilon$ from MSG, and ε_s from the WRF-Noah model. MSG surface spectral emissivity products were generated by LSA-SAF (2010) as a function of the (satellite-derived) fraction of vegetation cover (FVC) and land cover classification, at a daily frequency. Surface emissivity from WRF is a static terrestrial field which is function of the land-use type. Moreover, the effect of the leaf area index (LAI) and vegetation fraction (VEGFRAC) was implicitly taken into account when selecting λE, since these parameters are used to estimate the latent heat flux.

In order to identify specific relationships between the LST_{gt} results and the land cover definition, Fig. 13 plots the Pearson's correlation coefficient (r) obtained per pairs between the temporal mean LST_{gt} (Figs. 8 and 9) and the four aforementioned parameters. Pearson's r was calculated using pixels with LST_{gt} values above specific thresholds, defined every 0.1 K. VEGFRAC, LAI and ε_s were time-invariant fields during the period of study, whereas ε_{mean} from MSG was obtained daily. The variations of this parameter during the study period were not significant (standard deviation lower than 1%), therefore the temporal mean value was used to calculate r.

In BIASM, the correlations of the four parameters present similar trends for threshold values below 7 K with a maximum between 5 and 7 K, being r with VEGFRAC the highest. Pearson's coefficient has a maximum value around 0.4 for VEGFRAC, compared to the value of 0.25 for LAI and ε_{mean} and 0.17 for ε_s.

Fig. 13 (BIASM) shows also another correlation peak after 7.5 K for LAI and ε_s, which means that higher LST_{gt} values might be influenced by land cover definition (in this case, the WRF inputs). DMM presents a similar feature around 6.5 K, followed by inverse correlations (negative r) for higher LST_{gt} values. This may be related to the low number of values used in the correlation, namely 39, 25 and 6 for thresholds of 6.5, 7 and 7.5 K respectively, compared to a number of 157, 130 and 102 in BIASM.

For low threshold values (up to 2 K), LST_{gt} is mostly correlated with ε_{mean} in both models, although r is relatively low compared with the peak values in the graph. The correlation with ε_{mean} remains more or less stable in both models with values below 0.2.

5.8. Comparison with established method

5.8.1. Vaughan et al. (2012) method

The method described in Vaughan et al. (2012) and tested in the Yellowstone geothermal area was applied to the region of Olkaria geothermal field. This approach uses ASTER thermal infrared imagery at 90-m pixel resolution to calculate the radiant geothermal heat in thermal features after correcting for a background emittance. The ASTER data acquired on January 7th, 2012 at 20:09 UTC were used for this analysis.

As a first step, the location of geothermal features in the region was identified digitalizing information from a survey carried out by the Kenyan government and published in Clarke et al. (1990).

The area occupied by these features was divided into geographical subregions (namely north, northwest, central, south, and southeast) and a background area proximal to them with similar elevation and land cover properties was associated to each of them. Fig. 14a shows the ASTER LST product in Olkaria geothermal field where Lake Naivasha can be observed at the northeast part of the image. The location of geothermal features is indicated in yellow, orange, and red colors, and the backgrounds in blue. Different colors indicate that geothermal features were warmer than the associated mean background temperatures in 1, 2 or 3 standard deviations (σ) respectively. Fig. 14b shows a histogram of the ASTER surface temperature values in the northern

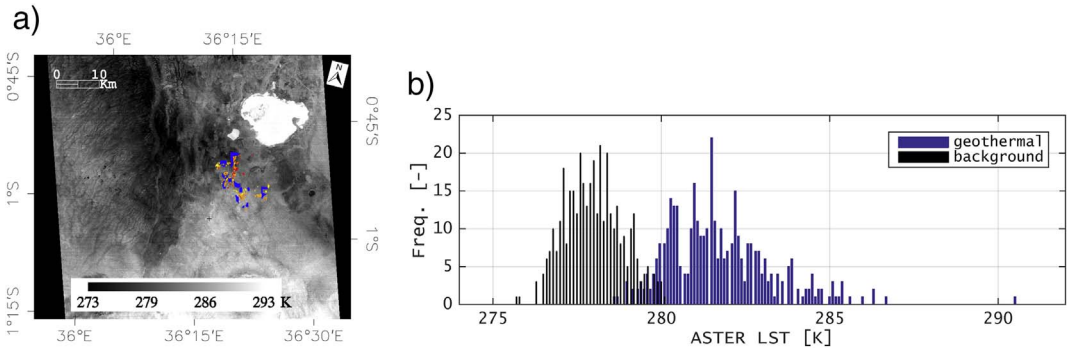

Fig. 14. (a) ASTER LST product in Olkaria region and location of reported geothermal features where colors indicate temperatures higher than the mean background (blue) plus 1σ (yellow), 2σ (orange) or 3σ (red), (b) histogram of values in the northern area (acquisition on January 7th, 2012 at 20:09 UTC). (For interpretation of the references to color in this figure legend, the reader is referred to the web version of this article.)

Table 3
Radiant geothermal flux obtained using Vaughan et al. (2012) in Olkaria subregions aggregating the results in 5 ranges, i.e. when the pixel LST value was higher than the mean background (BG) value plus 0, 1, 2, 3 and 4 standard deviations (σ).

Subregion	Radiant geothermal flux (W/m^2)				
	$LST > BG_{mean}$	$LST > BG_{mean} + 1\sigma$	$LST > BG_{mean} + 2\sigma$	$LST > BG_{mean} + 3\sigma$	$LST > BG_{mean} + 4\sigma$
North	18.6	19.6	19.3	21.5	23.9
Northwest	9.3	14.4	14.3	18.7	22.9
Central	9.8	12.1	11.8	14.1	17.8
South	10.9	15.4	13.0	15.9	20.0
Southeast	9.3	15.9	12.2	15.3	19.5

geothermal area.

For each area, surface temperatures from the AST08 data product were converted to radiant emittance (in W/m^2) using the Stephan-Boltzmann law and emissivity values from the AST05 data product. Mean background emittance was subtracted per subregion providing the radiant geothermal fluxes given in Table 3.

We examined 4 temperature threshold values for the thermal areas, corresponding to 1, 2, 3, and 4 standard deviations above the mean background (BG) temperature as indicated in Fig. 14a.

In general, higher values of radiant geothermal flux were found in the North subregion of Olkaria. The flux values ranged between 9 and 24 W/m^2 in the cases of the coldest ($LST > BG_{mean}$) and hottest ($LST > BG_{mean} + 4\sigma$) geothermal pixels respectively.

5.8.2. Application of BIASM and DMM

Fig. 15 shows the results of radiant geothermal flux obtained at 03:00 UTC in the Olkaria segment during the period 1st to 15th January, centered at the ASTER acquisition date, January 7th, 2012. Missing input data were found in Olkaria field between 16th and 23rd January 2012, as well as systematically higher LST_{gt} values during the second part of the study period, according to Fig. 7 and 11. Therefore, and in order to avoid the possible seasonal variability, a reasonable period of the first fifteen days was chosen to carry out the present validation. Although the results from Vaughan et al. (2012) were calculated at 20:09 UTC, in this paper priority was given to the use of the optimal analysis time, which is 03:00 UTC. Lake Naivasha and pixels with no data (due to clouds or no processed data) are masked in black. White color indicates negative LST_{gt} results which are labelled as non-geothermal pixels by the proposed approaches. The location of the geothermal features as analyzed in Section 5.8.1 are also plotted as a reference.

Fig. 15 shows that BIASM and DMM capture a local maximum in the location of the ground geothermal features. This pattern is consistent in time with radiant geothermal fluxes higher than 10 W/m^2 using BIASM, and lower in magnitude using DMM. BIASM produces relative maxima also in some northern areas. In these areas, according to the WRF datasets, land cover properties change, specifically, emissivity has a local maximum and albedo a local minimum. Other local geothermal flux maxima found in the southeast of the image coincide with the extent of local precipitation events occurred in the 24 h previous to the acquisition time.

In general, the series of radiant geothermal flux obtained in the pixels that contained ground geothermal features in BIASM was consistent with the ranges calculated in Section 5.8.1 using an established method. On January 7th, BIASM provided values between 10 and 15 W/m^2 and the method of Vaughan et al. (2012) computed a range between 9 and 24 W/m^2.

Since the spatial resolution of both analyses is substantially different (90 m for ASTER and 4 km for proposed approaches), the calculation of the total heat, after multiplying by the pixel area, will produce divergences in the results. The total heat obtained with ASTER by aggregating heat from sub regions was 188 MW, when using pixels whose

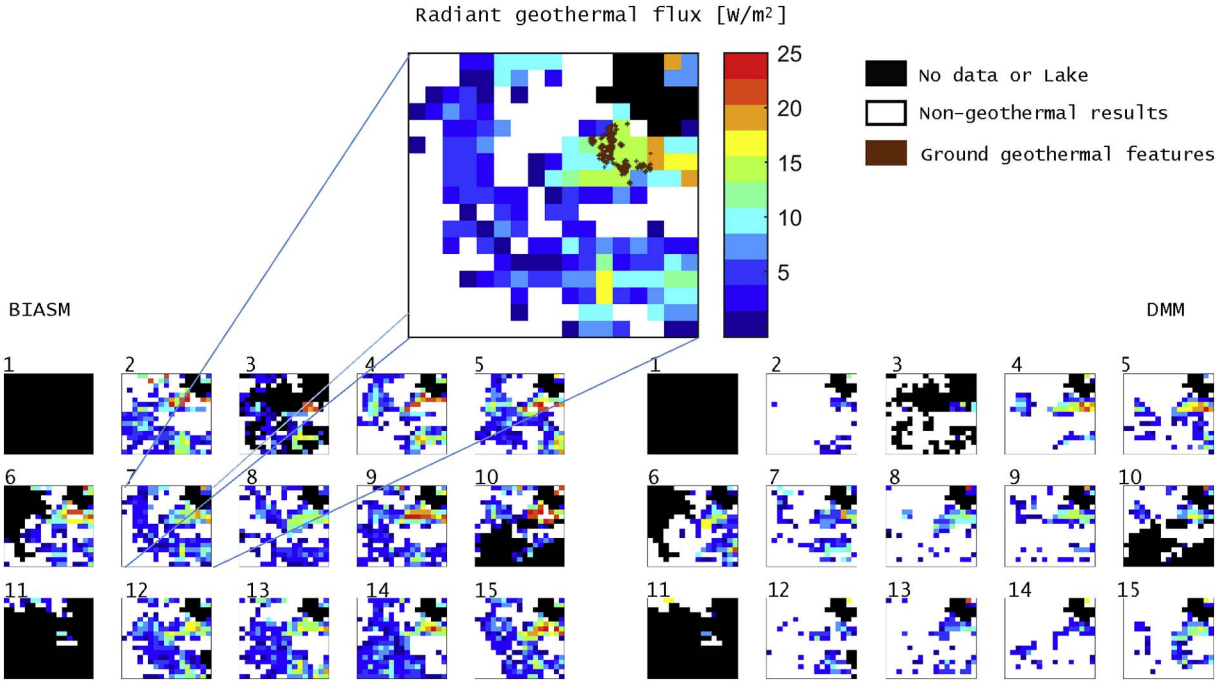

Fig. 15. (a) Radiant geothermal flux obtained with BIASM and DMM during the period 1st to 15th January 2012 (03:00 UTC) and close up on January 7th, 2012.

LST was larger than the background mean plus one standard deviation. This was the highest value obtained from all cases in Table 3. The value obtained from BIASM on January 7th 2012, by aggregating the heat from the pixels with ground geothermal features, was 6 times higher than the one obtained with ASTER. Reasons for these differences may be related to the spatial resolution of the analysis, since the proposed methods obtain the heat value for the whole 4×4 km^2 pixel whereas ASTER calculations are focused on locations with a priori knowledge of geothermal features. In this context, further research is needed to fully understand the subpixel thermal variability of the coarse pixels and the relationship with higher spatial resolution data. Other reasons may be related to methodological aspects such as the strategy to define background areas with ASTER, which is not standardized in the method. Finally, the uncertainties of the input parameters of the proposed models may play an important role in the final LST_{gt} estimations. This aspect is tackled in Section 6 of this paper.

6. Input uncertainties

This section describes the uncertainties of the main inputs used in the proposed approaches to estimate LST_{gt}, which are LST_{MSG} and LST_{WRF}.

The remote sensing LST_{MSG} products are distributed with an uncertainty estimated on a pixel-by-pixel basis, which accounts for the uncertainties of the algorithm and propagation of input errors. Freitas et al. (2010) indicated that dry atmospheres present LST_{MSG} uncertainties between 0.2 and 3.4 K, with a maximum in the uncertainty histogram in the range of 1 to 1.5 K. The total error depends in that case on emissivity uncertainties and to a lesser extent on the view zenith angle. For higher water vapor values, the distributions of uncertainties tend to be shifted to the right, maintaining the maximum between 1 and 1.5 K and reaching values up to 4.2 K.

Fig. 16 shows the mean error value during the period of analysis, using acquisitions at 03:00 UTC. The locations of the geothermal areas given by Omenda (2010) are included as a reference. The figure shows that MSG values are provided with an error lower than 2 K in most of the study area. Higher error values were found in specific areas at the east, west and south of Turkana lake (north) which correspond to areas with low emissivity values ($\varepsilon_{mean} < 0.97$), according to the MSG dataset. Moreover, the presence of (quartz) sand along the coast of Lake Turkana can produce mixed pixels along the shore with changing fractions of land and lake, causing emissivity uncertainties. In the areas indicated as geothermal by Omenda (2010), errors were lower than 1.7 K in the majority of them. The two northern areas fell in the region of the aforementioned lower emissivity values, and presented LST error values up to 2.2 K.

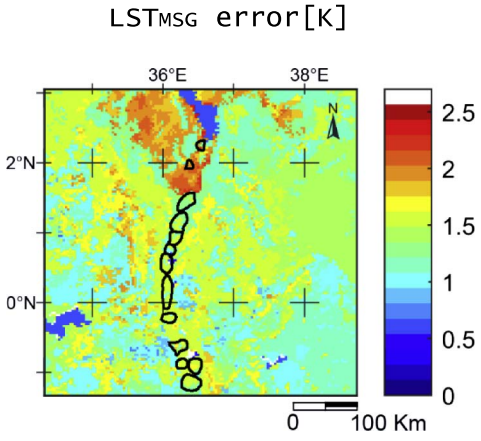

Fig. 16. Mean LST_{MSG} error during the period of analysis, using acquisitions at 03:00 UTC.

The uncertainty in LST_{WRF} estimations was assessed by comparing the model outputs with products available from the Global Land Data Assimilation System (GLDAS) (Rodell et al., 2004). These are obtained using also the Noah model at a resolution of 0.25° (about 25 km at the equator) but with different forcing and land cover datasets and assimilation techniques. Spatial aggregation of the 4 km WRF simulation outputs was undertaken to compute the differences at a coarse resolution. Fig. 17 shows the temporal mean and standard deviation of the difference LST_{WRF} minus LST_{GLDAS}. Lakes Turkana and west Victoria are masked in white color. Note that due to the scaling process a more extent area is masked next to the lakes and in the east and southern boundaries of the study area.

Regarding the mean value, most of the study area values range between -3 and 3 K (colors yellow and green). These areas present in general terms standard deviation values below 1.5 K which is an indicator of the consistency of the retrievals in time. Higher discrepancies are found in southern areas and in the East (colors orange and red), where higher variability in σ is also obtained. In the mid part and East of the study area LST_{WRF} are up to 9 K lower than LST_{GLDAS}. These areas partially coincide with anomalous high LST_{gt} values found in this paper (see Figs. 8 and 9). In particular, in the geothermal areas indicated by Omenda (2010), the mean difference value ranged between 4 and -4 K approximately, with standard deviation values up to 1.5 K in some areas. These results indicate that in some cases, the LST_{gt} method might be in the limit of detection when the input errors have the same or higher magnitude than the obtained LST_{gt}. An improvement in the input accuracies is therefore of crucial importance in the proposed research. Bearing in mind that both GLDAS and the generated WRF data have errors and limitations, further research is needed to fully understand the inconsistencies between these datasets.

7. Discussion

This section describes aspects to be taken into account when interpreting the results obtained in this paper regarding the inputs, approaches, assumptions, test and generalization.

Regarding the inputs, as indicated in Section 6 they have an important impact on the accuracy of the LST_{gt}. Particularly, the magnitude of the LST_{WRF} errors suggests the need of a comprehensive evaluation of different land surface model and LST outputs differences in the chosen study areas. Some works in that direction have been carried out by different authors (Jimenez et al., 2011; Kato et al., 2007; Robock et al., 2003). Although in some cases the determination of LST_{gt} might be hampered by these inaccuracies, the methods proposed in this paper remain valid and provide a framework where input improvements can be incorporated. Moreover, specific input parameters in the WRF model were assumed to be constant. Incorporating surface albedo and emissivity values that are dynamic in time would improve the definition of the land cover and representation of the surface states.

From a technical point of view, the rescaling and resampling of the input data to achieve a common spatial resolution may have an impact in the analysis. The nearest neighbor resampling technique was used in this research. In general, impacts on the results are expected due to the heterogeneity of the surface. The question of how representative is the low resolution data disaggregated to a higher scale needs further research.

In this paper, we prioritized the high temporal frequency of the data over the spatial resolution. The study was carried out at a spatial resolution of 4–5 km, which might limit the detection of small or less powerful geothermal features. However, the use of high temporal resolution data allowed monitoring the study area daily and obtain statistics during the study period (45 days). Moreover, high frequency data allows overcoming the problem of temporary cloudy pixels, since alternative clear sky acquisitions close to the optimal time can be used for the analysis.

Regarding the optimal analysis time, selection of night time data

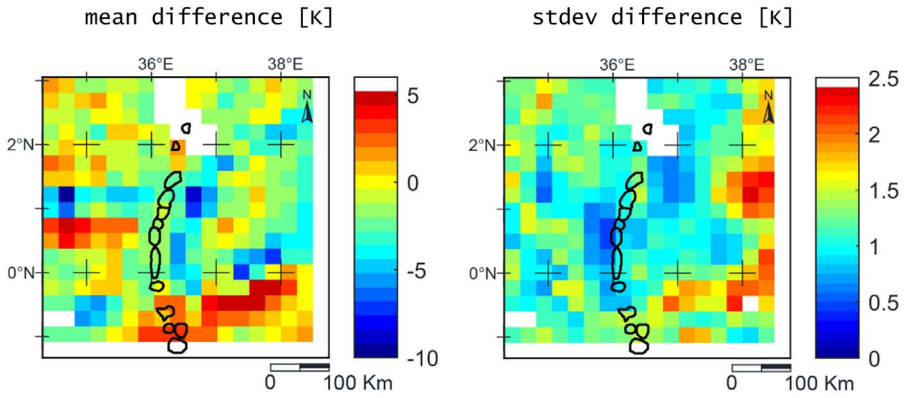

Fig. 17. Temporal mean and standard deviation of the difference LST_{WRF} minus LST_{GLDAS} during the period of analysis.

close and prior to sunrise were proposed in this paper. Bearing in mind that this represents the use of a single value of LST's and ancillary parameters per day, an alternative choice could be the use of averaged values prior to sun rise in order to avoid fluctuations.

The results showed the existence of anomalous high LST_{gt} values in complex terrain areas, which are false positives. In zones of complex topography, variability in elevation, surface slope, and aspect create strong spatial heterogeneity in solar distribution, which determines air temperature, soil temperature, evapotranspiration, snow melt and land–air exchanges. Therefore, LST_{MSG} satellite retrievals may need a slope and aspect correction to radiation inputs in these areas of significant relief, in order to provide more realistic results. Moreover, the uncertainty analysis revealed high LST_{WRF} errors in areas coincident with anomalous high LST_{gt}. Other LST_{gt} outliers were found in the time series during precipitation events or short after rainy days due to inherent patchy clouds. These aspects are consistent with the results of Sohrabinia et al. (2012). Similarly, an elevation correction (Eneva and Coolbaugh, 2009) might allow understanding the relative maxima present in the whole study area.

LST_{gt} values lower than zero were also obtained with the proposed models. These were related by hypothesis to non-geothermal pixels, when remote sensing LST's were not sufficiently higher than model simulations. The number of positive and negative values in the time series could be used as indicators of the reliability of the results, and could suggest the need of a more extensive time series analysis. The ratio between temporal positive mean and temporal negative mean indicated also the significance of these negative values, which was higher than 100% in non-geothermal areas.

The analysis of vegetation definition showed that LST_{gt} was correlated ($r = 0.4$) to the fraction of vegetation cover with maxima around 6 and 4 K in BIASM and DMM. For higher LST_{gt} threshold values the results indicated a correlation with LAI and emissivity from WRF. These results suggest that LST_{gt} peak values could be partially influenced by vegetation definition, and be shown as false geothermal positives.

Regarding the proposed approaches, from an operative point of view BIASM is recommended, since it is simple and has a straightforward application. It allows to produce long-term results at high temporal frequencies and no apriori information about geothermal anomalies is needed. The synergy of this method with Vaughan et al.'s (2012) method would benefit from the spatial resolution of the latter.

The assumptions and choices made in this work might influence the uncertainty of the results. The $bias_{LST}$ values in BIASM might fluctuate if other thresholds for mapping reference areas would have been chosen, or if the segmentation would have been different. Regarding the parameters chosen for the clustering and prediction, the choices were justified in the corresponding section of this paper, however, a sensitivity analysis could have been used to select the optimal set to describe the study area. The number of clusters was set to the default value of 5, however, a different approach where the optimal number of clusters is calculated could have been adopted as detailed in Rezaee et al. (1998) and implemented in Romaguera et al. (2014). Moreover, the results are influenced by the land surface model selected. An intercomparison of different LST model outputs would contribute to the assessment of this influence.

The strategy followed in this paper to validate the approaches was based on the comparison of the radiant geothermal flux (equivalent to LST_{gt}) with the one obtained with an established method in the Olkaria geothermal area. The results indicated that in general, the values obtained with the two analysis were consistent, providing radiant geothermal fluxes between 9 and 24 W/m^2. Fluctuations in the difference values might be due to methodological and technical aspects. First, Vaughan et al. (2012) begins the analysis with an apriori knowledge of the location of the geothermal features and areas, for which the radiant geothermal flux is calculated. In the presented approaches, the radiant geothermal flux is obtained for all the areas, which may include additional not cataloged thermal anomalies, and therefore obtain higher geothermal heat values. Regarding specific properties of the study areas, complex topography or high atmospheric water vapor content might influence both estimates. Complex topography influences the LST detection signal, and steam is a key atmospheric component that highly influences the atmospheric correction for LST retrieval. The accuracy of the inputs plays also an important role in the interpretation of the results. Finally, the comparison was carried out using data at two different times, namely 03:00 and 20:09 UTC in the proposed and established methods respectively. In this paper, priority was given to calculations at the optimal night time (03:00 UTC) to minimize sun heating effects. Contrarily, these have a higher influence on ASTER acquisitions at 20:09 UTC due to the thermal inertia of the surface, which might cause deviations from the optimal heat outcomes.

The proposed approach has the advantage of the high temporal frequency of the inputs and does not need any apriori information about the location of geothermal areas, whereas the method of Vaughan et al. (2012) has the advantage of higher spatial resolution data and the ability to detect more subtle geothermal features. Bearing in mind these issues, a synergy between both would provide tools to monitor geothermal activity at a relevant time and spatial scales.

The generalization of the proposed approaches to other areas, periods of time and datasets is feasible as long as the main hypothesis is accomplished. Remote sensing LST formulation must include the geothermal component, contrary to model simulations. Remotely derived LST datasets at large scale can be obtained from sources such as the MOD11 LST MODIS dataset, the European Copernicus Global Land Service (Freitas et al., 2013) or the LST products from the GlobTemperature project (http://data.globtemperature.info/). LST model simulations are globally available using different schemes from the Global Land Data Assimilation System (GLDAS) (Rodell et al., 2004), at coarse resolutions. In this context, limitations are related to the lack of available operative high spatial resolution model simulations. For specific study cases, a preliminary analysis is needed to evaluate the physics of the processes at the desired resolution, and the proper approach for LST

modeling.

Finally, this paper focused on analyzing the land surface temperature as an indicator of geothermal activity. However, geochemical and geophysical information, such as mineralogy alteration, gravity, and magnetics analysis, might be also included in the research, with the objective of constraining the outputs. A review about how geologic remote sensing has been used for geothermal exploration was recently published by van der Meer et al. (2014).

Despite the fact that more detailed analysis is required to draw more robust conclusions about the operationality of the presented approaches, this paper provided new tools and an initial framework to assess and monitor geothermal activity at appropriate temporal scales and large coverage.

8. Conclusions

In this paper, we propose two innovative approaches to obtain the geothermal component of LST (LST_{gt}) through the use of two LST time series; one is derived from geostationary Meteosat satellite (including the geothermal component) and one resulting from WRF land model simulations (neglecting the geothermal component). The originality of the two approaches lies in the high temporal frequency of the results, and that they do not require any apriori geothermal information for the area under investigation.

The first approach (BIASM) is based on calculating the LST differences between the remote sensing and WRF data sources and applying a $bias_{LST}$ correction. The approach is simple and has a straightforward application. The second approach (DMM) examines four machine learning techniques to predict remote sensing LST from simulated data. Of the four techniques, the *decision tree* resulted in the smallest errors and highest correlation coefficients.

The two approaches show consistent LST_{gt} patterns, with BIASM typically showing 2 K higher LST_{gt} values than DMM. A geothermal area map from surface studies is used to assess LST_{gt} inside and outside the geothermal boundaries. Spatial means are found to be higher inside the geothermal limits, as well as the relative frequency of occurrence of high LST_{gt}. Areas with strong topography can result in anomalous high LST_{gt} values, which suggests the need for a slope and aspect correction to achieve realistic results in those areas.

Our uncertainty analysis indicates the necessity for more consistent model LST_{WRF} retrievals. In some cases LST_{gt} detection might be limited by high inaccuracies of the input parameters (up to 4 K) in specific geothermal areas of the study region. Moreover, some anomalously high LST_{gt} values coincided with high LST_{WRF} error estimates in the same area.

The validation exercise provides similar radiant geothermal flux when comparing the proposed approaches (during 15 days) with an established method that uses ASTER data at higher spatial resolution (single acquisition), with values between 9 and 24 W/m^2. However, further research is needed to understand the subpixel thermal variability and the relationship with the outputs of this paper. Our results also indicate the potential of combining the high spatial resolution of the existing methods with the high temporal resolution of the ones proposed in this work.

The proposed methods are a first step in estimating LST_{gt} at large spatial coverage from remote sensing and land model simulation data, and provides an innovative framework for future improvements.

Acknowledgements

The authors wish to thank the Land Surface Analysis Satellite Applications Facility (LSA-SAF) of the European Organization for the Exploitation of Meteorological Satellites (EUMETSAT) for providing the products used in this paper.

We would like to acknowledge the University of Twente (The Netherlands) for offering Dr. M. Romaguera the time to work on this paper. The research by RGV described herein was carried out, in part, at the USGS Astrogeology Science Center in Flagstaff, AZ, with support from the USGS Geothermal Research Program and the USGS Volcano Hazards Program. Thanks also to the ASTER science team at JPL.

The authors wish to thank the editor J. M. Chen and the anonymous reviewer who have contributed to improve the manuscript, as well as Dr. J.P. Aguilar-López for his contribution in the graphical aspects of this paper.

References

Bertani, R., 2015. Installed capacity in 2015 worldwide. In: Credit: Geothermal Power Generation in the World 2010–2014 Update Report.

Bishop, C.M., 2007. Pattern Recognition and Machine Learning (Corr.printing ed.). Springer, New York (US).

Camps-Valls, G., Bruzzone, L., Rojo-Alvarez, J.L., Melgani, F., 2006. Robust support vector regression for biophysical variable estimation from remotely sensed images. IEEE Geosci. Remote Sens. Lett. 3, 339–343.

Caselles, V., Sobrino, J.A., 1989. Determination of frosts in orange groves from NOAA-9 AVHRR data. Remote Sens. Environ. 29, 135–146.

Clarke, M.C.G., Woodhall, D.G., Allen, D., Darling, G., 1990. Geological, volcanological and hydrogeological controls of the occurrence of geothermal activity in the area surrounding Lake Naivasha, Kenya. In: Energy, M.o. (Ed.), p. 348, (Nairobi).

Coolbaugh, M.F., Kratt, C., Fallacaro, A., Calvin, W.M., Taranik, J.V., 2007. Detection of geothermal anomalies using Advanced Spaceborne Thermal Emission and Reflection Radiometer (ASTER) thermal infrared images at Bradys Hot Springs, Nevada, USA. Remote Sens. Environ. 106, 350–359.

Dee, D.P., Uppala, S.M., Simmons, A.J., Berrisford, P., Poli, P., Kobayashi, S., Andrae, U., Balmaseda, M.A., Balsamo, G., Bauer, P., Bechtold, P., Beljaars, A.C.M., van de Berg, L., Bidlot, J., Bormann, N., Delsol, C., Dragani, R., Fuentes, M., Geer, A.J., Haimberger, L., Healy, S.B., Hersbach, H., Hólm, E.V., Isaksen, L., Kållberg, P., Köhler, M., Matricardi, M., McNally, A.P., Monge-Sanz, B.M., Morcrette, J.J., Park, B.K., Peubey, C., de Rosnay, P., Tavolato, C., Thépaut, J.N., Vitart, F., 2011. The ERA-Interim reanalysis: configuration and performance of the data assimilation system. Q. J. R. Meteorol. Soc. 137, 553–597.

Duda, R.O., Hart, P.E., Stork, D.G., 1998. Pattern Classification and Scene Analysis: Part I Pattern Classification, 2nd edition. John Wiley & Sons, New York (US).

Eneva, M., Coolbaugh, M., 2009. Importance of elevation and temperature inversions for the interpretation of thermal infrared satellite images used in geothermal exploration. GRC Transacions 33.

Eskandari, A., De Rosa, R., Amini, S., 2015. Remote sensing of Damavand volcano (Iran) using Landsat imagery: implications for the volcano dynamics. J. Volcanol. Geotherm. Res. 306, 41–57.

Exelis, 2013. ENVI Tutorial: Classification Methods. Exelis Visual Information Solutions, Boulder, Colorado.

Freitas, S.C., Trigo, I.F., Bioucas-Dias, J.M., Gottsche, F.M., 2010. Quantifying the uncertainty of land surface temperature retrievals from SEVIRI/Meteosat. IEEE Trans. Geosci. Remote Sens. 48, 523–534.

Freitas, S.C., Trigo, I.F., Macedo, J., Barroso, C., Silva, R., Perdigao, R., 2013. Land surface temperature from multiple geostationary satellites. Int. J. Remote Sens. 34, 3051–3068.

Gillespie, A., Rokugawa, S., Matsunaga, T., Cothern, J.S., Hook, S., Kahle, A.B., 1998. A temperature and emissivity separation algorithm for Advanced Spaceborne Thermal Emission and Reflection Radiometer (ASTER) images. IEEE Trans. Geosci. Remote Sens. 36, 1113–1126.

Gutierrez, F.J., Lemus, M., Parada, M.A., Benavente, O.M., Aguilera, F.A., 2012. Contribution of ground surface altitude difference to thermal anomaly detection using satellite images: application to volcanic/geothermal complexes in the Andes of Central Chile. J. Volcanol. Geotherm. Res. 237, 69–80.

Haselwimmer, C., Prakash, A., 2013. Thermal infrared remote sensing of geothermal systems. In: Kuenzer, C., Dech, S. (Eds.), Thermal Infrared Remote Sensing: Sensors, Methods, Applications. Springer, Dordrecht, pp. 17.

Hastie, T., Tibshirani, R., DFriedman, J., 2009. The Elements of Statistical Learning: Data Mining Inference and Prediction.

Haykin, S., 1999. Neural Networks: A Comprehensive Foundation. Prentice Hall, Englewood Cliffs (US).

Hochstein, M.P., Kagiri, D., 1997. The role of 'steaming ground' over high temperature systems in the Kenya Rift. In: Twenty-First Workshop on Geotheram Reservoir Engineering. Standford University, Standford, California.

Jimenez, C., Prigent, C., Mueller, B., Seneviratne, S.I., McCabe, M.F., Wood, E.F., Rossow, W.B., Balsamo, G., Betts, A.K., Dirmeyer, P.A., Fisher, J.B., Jung, M., Kanamitsu, M., Reichle, R.H., Reichstein, M., Rodell, M., Sheffield, J., Tu, K., Wang, K., 2011. Global intercomparison of 12 land surface heat flux estimates. J. Geophys. Res.-Atmos. 116, 27.

Kato, H., Rodell, M., Beyrich, F., Cleugh, H., van Gorsel, E., Liu, H.Z., Meyers, T.P., 2007. Sensitivity of land surface simulations to model physics, land characteristics, and forcings, at four CEOP sites. J. Meteorol. Soc. Jpn. 85A, 187–204.

King, D., Metcalfe, E., 2013. Rift zones as a case study for advancing geothermal occurrence models. In: Thirty-eight Workshop on Geothermal Reservoir Engineering. Standford University, Standford, California.

LSA-SAF, 2010. Product user manual. Land surface temperature (LST). In: The EUMETSAT Network of Satellite Application Facilities, (Doc. num. SAF/LAND/IM/

PUM_LST/2.5).
Mutua, J., Friese, A., Kuehn, F., Lopeyok, T., Mutonga, M., Ochmann, N., 2013. High resolution airborne thermal infrared remote sensing study, Silali geothermal prospect, Kenya. In: Presented at Short Course VIII on Exploration for Geothermal Resources, Organized by UNU-GTP, GDC and KenGen, at Lake Bogoria and Lake Naivasha, Kenya, Oct. 31–Nov. 22, 2013.
Niu, G.Y., Yang, Z.L., Mitchell, K.E., Chen, F., Ek, M.B., Barlage, M., Kumar, A., Manning, K., Niyogi, D., Rosero, E., Tewari, M., Xia, Y.L., 2011. The community Noah land surface model with multiparameterization options (Noah-MP): 1. Model description and evaluation with local-scale measurements. J. Geophys. Res.-Atmos. 116, 19.
NWC-SAF, 2010. Algorithm theoretical basis document for SAFNWC/PPS "Cloud Mask" (CMPGE01 v3.0-patch1). In: The EUMETSAT Network of Satellite Application Facilities, (Doc. Num. SAF/NWC/CDOP/SMHI-PPS/SCI/ATBD/1).
Omenda, P.A., 2010. Geothermal exploration in Kenya. In: Presented at Short Course V on Exploration for Geothermal Resources, organized by UNU-GTP, GDC and KenGen, at Lake Bogoria and Lake Naivasha, Kenya, Oct. 29–Nov. 19, 2010.
Pastor, M.S., 2010. Application of Thermal Remote Sensing for Geothermal Mapping, Lake Naivasha, Kenya. World Geothermal Congress, Bali, Indonesia.
Peres, L.F., DaCamara, C.C., 2005. Emissivity maps to retrieve land-surface temperature from MSG/SEVIRI. IEEE Trans. Geosci. Remote Sens. 43, 1834–1844.
Qin, Q.M., Zhang, N., Nan, P., Chai, L.L., 2011. Geothermal area detection using Landsat ETM plus thermal infrared data and its mechanistic analysis-a case study in Tengchong, China. Int. J. Appl. Earth Obs. Geoinf. 13, 552–559.
Quinlan, R.J., 1993. C4.5: Programs for Machine Learning. Morgan Kaufman Publishers Inc, San Mateo, California.
Ramsey, M.S., Harris, A.J.L., 2013. Volcanology 2020: how will thermal remote sensing of volcanic surface activity evolve over the next decade? J. Volcanol. Geotherm. Res. 249, 217–233.
Rezaee, M.R., Lelieveldt, B.P.F., Reiber, J.H.C., 1998. A new cluster validity index for the fuzzy c-mean. Pattern Recogn. Lett. 19, 237–246.
Robock, A., Luo, L.F., Wood, E.F., Wen, F.H., Mitchell, K.E., Houser, P.R., Schaake, J.C., Lohmann, D., Cosgrove, B., Sheffield, J., Duan, Q.Y., Higgins, R.W., Pinker, R.T., Tarpley, J.D., Basara, J.B., Crawford, K.C., 2003. Evaluation of the North American Land Data Assimilation System over the southern Great Plains during the warm season. J. Geophys. Res.-Atmos. 108, 21.
Rodell, M., Houser, P.R., Jambor, U., Gottschalck, J., Mitchell, K., Meng, C.J., Arsenault, K., Cosgrove, B., Radakovich, J., Bosilovich, M., Entin, J.K., Walker, J.P., Lohmann, D., Toll, D., 2004. The global land data assimilation system. Bull. Am. Meteorol. Soc. 85, 381–394.
Romaguera, M., Krol, M.S., Salama, M.S., Hoekstra, A.Y., Su, Z., 2012. Determining irrigated areas and quantifying blue water use in Europe using remote sensing Meteosat Second Generation (MSG) products and Global Land Data Assimilation System (GLDAS) data. Photogramm. Eng. Remote. Sens. 78, 861–873.
Romaguera, M., Salama, S., Krol, M.S., Hoekstra, A.Y., Su, Z., 2014. Towards the improvement of blue evapotranspiration estimates by combining remote sensing and model simulation. Remote Sens. 6, 7026–7049.
Skamarock, W.C., Klemp, J.B., Dudhia, J., Gill, D.O., Barker, D.M., Duda, M.G., Huang, X.Y., Wang, W., Powers, J.G., 2008. A Description of the Advanced Research WRF Version 3.
Sohrabinia, M., Rack, W., Zawar-Reza, P., 2012. Analysis of MODIS LST compared with WRF model and in situ data over the Waimakariri River Basin, Canterbury, New Zealand. Remote Sens. 4, 3501–3527.
Teklemariam-Zemedkun, M., 2011. Overview of geothermal resource exploration and development in the East African Rift system. In: Presented at Short Course VI on Exploration for Geothermal Resources, Organized by UNU-GTP, GDC and KenGen, at Lake Bogoria and Lake Naivasha, Kenya, Oct. 27–Nov. 18, 2011.
Tou, J.T., Gonzalez, R.C., 1974. Pattern Recognition Principles. Addison-Wesley Publishing Company, Reading, Massachusetts.
van der Meer, F., Hecker, C., van Ruitenbeek, F., van der Werff, H., de Wijkerslooth, C., Wechsler, C., 2014. Geologic remote sensing for geothermal exploration: a review. Int. J. Appl. Earth Obs. Geoinf. 33, 255–269.
Vapnik, V.N., 1998. Statistical Learning Theory. John Wiley & Sons, New York (US).
Vaughan, R.G., Keszthelyi, L.P., Lowenstern, J.B., Jaworowski, C., Heasler, H., 2012. Use of ASTER and MODIS thermal infrared data to quantify heat flow and hydrothermal change at Yellowstone National Park. J. Volcanol. Geotherm. Res. 233–234, 72–89.
Wan, Z.M., Dozier, J., 1996. A generalized split-window algorithm for retrieving land-surface temperature from space. IEEE Trans. Geosci. Remote Sens. 34, 892–905.
Watson, F.G.R., Lockwood, R.E., Newman, W.B., Anderson, T.N., Garrott, R.A., 2008. Development and comparison of Landsat radiometric and snowpack model inversion techniques for estimating geothermal heat flux. Remote Sens. Environ. 112, 471–481.
WRF, 2012. Weather Research & Forecast WRF ARW. Version 3 Modeling System User's Guide. National Center for Atmospheric Research.
Zeng, X.M., Wang, N., Wang, Y., Zheng, Y.Q., Zhou, Z.G., Wang, G.L., Chen, C.H., Liu, H.Q., 2015. WRF-simulated sensitivity to land surface schemes in short and medium ranges for a high-temperature event in East China: a comparative study. J. Adv. Model. Earth Syst. 7, 1305–1325.